A Lagrangian Perspective on Parameterizing Deep Convection

RON MCTAGGART-COWAN, PAUL A. VAILLANCOURT, AYRTON ZADRA, AND LEO SEPAROVIC

Atmospheric Numerical Weather Prediction Research Section, Environment and Climate Change Canada, Dorval, Quebec, Canada

SHAWN CORVEC

Numerical Weather Prediction Development, Environment and Climate Change Canada, Dorval, Quebec, Canada

DANIEL KIRSHBAUM

Department of Atmospheric and Oceanic Sciences, McGill University, Montreal, Quebec, Canada

(Manuscript received 28 May 2019, in final form 1 August 2019)

ABSTRACT

The parameterization of deep moist convection as a subgrid-scale process in numerical models of the atmosphere is required at resolutions that extend well into the convective ''gray zone,'' the range of grid spacings over which such convection is partially resolved. However, as model resolution approaches the gray zone, the assumptions upon which most existing convective parameterizations are based begin to break down. We focus here on one aspect of this problem that emerges as the temporal and spatial scales of the model become similar to those of deep convection itself. The common practice of static tendency application over a prescribed adjustment period leads to logical inconsistencies at resolutions approaching the gray zone, while more frequent refreshment of the convective calculations can lead to undesirable intermittent behavior. A proposed parcel-based treatment of convective initiation introduces memory into the system in a manner that is consistent with the underlying physical principles of convective triggering, thus reducing the prevalence of unrealistic gradients in convective activity in an operational model running with a 10 km grid spacing. The subsequent introduction of a framework that considers convective clouds as persistent objects, each possessing unique attributes that describe physically relevant cloud properties, appears to improve convective precipitation patterns by depicting realistic cloud memory, movement, and decay. Combined, this Lagrangian view of convection addresses one aspect of the convective gray zone problem and lays a foundation for more realistic treatments of the convective life cycle in parameterization schemes.

1. Introduction

Numerical models are necessarily limited in their ability to resolve the broad range of scales over which physical processes in the atmosphere occur. As a result, these processes must be parameterized such that their impacts on the resolved-scale state can be represented as accurately as possible. When the grid spacing of the numerical model is fine enough to resolve a given physical process completely, ''scale-aware'' schemes naturally become inactive (Arakawa and Schubert 2011; Grell and Freitas 2014; Han et al. 2017), while traditional schemes are explicitly deactivated. Problems arise, however, at intermediate grid spacings when portions of the atmospheric process begin to be resolved, while others remain strictly subgrid scale (Wyngaard 2004). Over this range of ''gray zone'' resolutions, the fundamental assumptions upon which parameterizations are based may become increasingly invalid, leading to unphysical behavior in the scheme and the development of important errors in depiction of the resolved-scale flow.

One of the first gray zone problems to be encountered by operational NWP systems is associated with the parameterization of deep convection, for which grid spacings on the order of 1–10 km pose a significant challenge

Denotes content that is immediately available upon publication as open access.

Corresponding author: Ron McTaggart-Cowan, ron.mctaggart-cowan@canada.ca

DOI: 10.1175/MWR-D-19-0164.1

(Molinari and Dudek 1992; Arakawa 2004). At such scales, it is impossible to cleanly separate cloud properties from the environmental conditions without an explicit estimate of the updraft area fraction of the kind proposed by Gerard and Geleyn (2005) and Arakawa and Wu (2013). As an increasing fraction of the grid cell is occupied by the updraft, it becomes clear that compensating subsidence needs to be considered in neighboring grid volumes. Kuell et al. (2007) propose a hybridized approach in which the net mass flux of the convective updrafts and downdrafts are evaluated within a grid cell by the parameterization, while compensating subsidence is handled by the model dynamics. The convective motions themselves begin to be resolved as kilometer-scale grid spacing is employed. However, Bryan et al. (2003) demonstrate that although models with a 1 km grid spacing are capable of reproducing the general structure of the convective features, the relevant turbulent motions are not resolved until the grid spacing is reduced to 100 m or less. This extension of the convective gray zone into the realm of current large eddy simulation resolutions is further supported by the analyses of Stevens et al. (2002), Craig and Dörnbrack (2008) and Bryan and Morrison (2012), suggesting that problems associated with the parameterization of at least some aspects of moist convection will be faced by NWP models for at least the foreseeable future (Hong and Dudhia 2012).

In addition to these spatial problems, model time scales that become shorter than those associated with deep convection pose a challenge for traditional convective schemes that rely on the assumption of a quasi equilibrium between the large-scale forcing and the convective response (Arakawa and Shubert 1974; Bougeault and Geleyn 1989; Mapes 1997; Cohen and Craig 2006). Zimmer et al. (2011) show that roughly one-third of warm-season convective precipitation events in Germany are nonequilibrium in nature, and that such cases are associated with systematic errors in the NWP guidance produced by a mesoscale model using parameterized convection (Tiedtke 1989; Steppeler et al. 2003). The failure of equilibrium assumptions as the forcing time scale approaches that of convection is further quantified by Jones and Randall (2011), who use a high-resolution model in a semi-idealized configuration to conclude that even the diurnal cycle can introduce important nonequilibrium effects. Although Davies et al. (2013) argue that the diurnal cycle can generate locally organized convection that is in quasi equilibrium, their simulations show appreciable nonequilibrium behavior for forcing time scales on the order of 3–12 h. Although recent convective schemes are designed to detect such cases in which the convective calculations should be refreshed more frequently (Bechtold et al. 2008), this solution can lead to intermittent activation in weakly unstable cases (Gerard et al. 2009).

The spatiotemporal problems in the convective gray zone converge on the issue of representing the life cycles of deep convective clouds (Gerard 2015). Traditional schemes rely on a statistical equilibrium of convection within a grid cell for which a mean ''mature'' state is applicable (Arakawa and Shubert 1974). However, as the resolved scales collapse toward those of individual clouds it is clear that convective growth, maturity and decay phases of the cloud life cycle should be depicted by the parameterization (Gerard et al. 2009). The introduction of prognostic equations for specific cloud properties such as convective kinetic energy (Pan and Randall 1998) and updraft speed (Gerard and Geleyn 2005) establishes a framework for such a realistic representation of convective cloud evolution by introducing a ''memory effect'' (Davies et al. 2013). The concept of convective memory is investigated in detail by Colin et al. (2019), who use a cloud resolving model within a typical climate model grid cell to evaluate the time taken to restore radiative-convective equilibrium after the removal of subgrid-scale variability (''microstructure''). They show that the memory of convective systems lies largely in their perturbations to subcloud thermodynamic structures, with the associated time scales varying from a few hours to a day depending primarily on convective organization.

In this study, we build on these cloud-scale concepts to develop a Lagrangian view of deep convection that applies to both convective initiation and the evolution of convective cloud objects. The perspective is conceptually separate from the formulation of the parameterization itself, meaning that the framework described here may be adopted to introduce memory into a range of convective schemes employed at resolutions nearing or within the gray zone. We begin with a description of the existing convective parameterization used in the Canadian NWP model in section 2. A case study of heavy precipitation in the Caribbean region is introduced in section 3, and used thereafter to examine the sensitivity of parameterized convection to a Lagrangian treatment of convective initiation (section 4) and the introduction of convective cloud objects (section 5). The study concludes with a discussion of the results in sections 6 and 7, wherein we note the potential for this framework to be extended to include cloud-specific prognostic equations to improve the representation of the cloud life cycle within the convective gray zone.

2. Data and methods

a. Model description

The Canadian Global Environmental Multiscale (GEM) model is employed throughout this study. This model is used in all operational NWP applications run at the Canadian Meteorological Centre to provide guidance to forecasters on scales from global (~39 km grid spacing) to local (~2.5 km grid spacing). Girard et al. (2014) describe the updated implicit, semi-Lagrangian dynamical core for GEM that solves the governing equations on a latitude–longitude Arakawa C grid. The vertical log-hydrostatic pressure, terrain-following coordinate is discretized following Charney and Phillips (1953).

The configuration used here is a form of the operational Regional Deterministic Prediction System that is scheduled for operational implementation in the summer of 2019. The domain for this system covers most of the Western Hemisphere north of the equator with a grid spacing of 0.09° (~10 km), placing it at the upper end of the convective "gray zone" (Tomassini et al. 2017; Field et al. 2017). The model's 84 vertical levels are most tightly spaced near the lowest 10-m thermodynamic level, with 19 levels below 850 hPa over the ocean. Vertical resolution decreases slowly with height in the troposphere and more rapidly in the stratosphere such that layers near the 0.1 hPa model lid are approximately 1 km thick.

The physical parameterization package in this GEM configuration has undergone important updates in recent years, the details and impacts of which are described by McTaggart-Cowan et al. (2019, manuscript submitted to *Mon. Wea. Rev.*). A modified form of the Interactive Soil–Biosphere–Atmosphere (Noilhan and Planton 1989; Bélair et al. 2003a,b) land surface scheme evolves the terrestrial lower boundary condition, while the 1D ocean mixed layer model proposed by Zeng and Beljaars (2005) is used to represent the diurnal cycle of sea surface temperature. Updates to the Li and Barker (2005) radiative transfer scheme have impacts on stratospheric temperatures, but do not affect the results described here; nor do modifications to the Zadra et al. (2003) blocking and McFarlane (1987) orographic gravity wave drag parameterizations. However, a reduction of the effects of turbulent mixing in stratocumulus clouds and the use of the Bougeault and Lacarrère (1989) mixing length in turbulent regimes represent important changes to the Bélair et al. (2005) boundary layer scheme that affect convective activity. Likewise, the adoption of the Bechtold et al. (2001) mass-flux scheme to represent the effects of shallow cumulus has an impact on the development of the convective instability required for the initiation and maintenance of deep convective clouds as represented by the model's convection parameterization [based on Kain and Fritsch (1990, 1992)]. Although it is changes to the latter that are the focus of this investigation, direct interaction also occurs between the convection and gridscale condensation schemes in the form of condensate detrainment from cloud updrafts. However, the Sundqvist et al. (1989) condensation scheme was one of the few components of physics package that did not undergo significant modification during this update.

b. Overview of current deep convective scheme

Deep convection is parameterized in all Canadian operational models using a form of the Kain and Fritsch (1990, 1992) convection parameterization. Although many of the details of the scheme have evolved since its initial implementation in the GEM model, the fundamental components of the original formulation remain intact (Zadra et al. 2014). Because the majority of these elements are shared with other moist convective schemes (both deep and shallow), most of the discussions in the subsequent sections of this study will be readily extensible to other implementations of mass-flux-based convective parameterizations. Readers already familiar with such schemes may wish to proceed directly to section 2c.

In its simplest form, the convective scheme can be considered to consist of three primary building blocks: a "trigger," a plume model, and a closure (Fig. 1). The first of these is of particular relevance to this study because it determines whether or not the parameterization is active at each grid point on the model domain. The formulation of the trigger in GEM is based on the Fritsch and Chappell (1980) design as described by Kain and Fritsch (1992), a framework intended to represent convective initiation by boundary layer thermals rising in an environment of large-scale ascent. Starting at the surface, parcels are created by mixing over a layer of minimum 60 hPa depth: the "updraft source layer." Each parcel undergoes undilute ascent to its lifting condensation level (LCL), where its properties are compared to those of the local environment to determine whether it will continue to rise once condensation begins.

The stability of a parcel at the LCL is strongly influenced by resolved-scale ascent in the Fritsch and Chappell (1980) formulation of the convective trigger function in GEM. Designed to represent the destabilizing effects of synoptic or mesoscale ascent on the subcloud thermodynamic profile, this dependence is implemented as a temperature perturbation applied to parcels at the LCL:

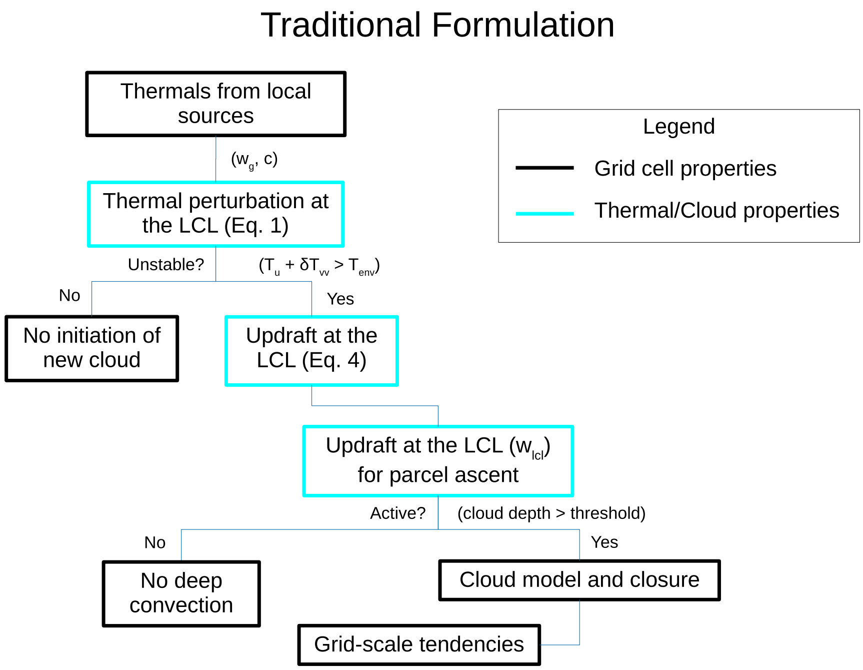

FIG. 1. Schematic of the existing Kain and Fritsch (1990, 1992)–based convective parameterization scheme used in the GEM model.

$$\delta T_{vv} = k[w_g - c(\mathbf{X},t)]^{1/3}. \tag{1}$$

In this characterization of the properties of rising unresolved thermals, $k = 4.64\,\mathrm{K\,s^{1/3}\,m^{-1/3}}$ and the threshold[1] vertical velocity $c(\mathbf{X}, t)$ is a function of both space ($\mathbf{X}$) and time (t). Kain (2004) notes that the resolved vertical motion at the LCL (w_g) should be a running mean of the gridscale vertical motion for consistency with the "resolved" nature of the ascent; however, the implementation in GEM is based on the instantaneous value, thus rendering Eq. (1) purely diagnostic.

The activity of the convective scheme is highly dependent on the value selected for c, which in this configuration of GEM is a constant over land ($c_{\mathrm{land}} = 0.2\,\mathrm{m\,s^{-1}}$) and over ocean depends on the convective velocity scale (w_*) as

$$c_{\mathrm{ocean}} = \begin{cases} A\,, & \text{for} \quad w_* \le w_{*A} \\ A + (B-A)\dfrac{w_* - w_{*A}}{w_{*B} - w_{*A}}, & \text{for} \quad w_{*A} < w_* < w_{*B}\,, \\ B\,, & \text{for} \quad w_* \ge w_{*B} \end{cases} \tag{2}$$

where

$$w_* = \left[\frac{g z_i}{T_v}(\overline{w'\theta_v'})_s\right]^{1/3}, \tag{3}$$

$A = 0.1$, $B = 0.02$, $w_{*A} = 0.5$, and $w_{*B} = 1\,\mathrm{m\,s^{-1}}$ in the configuration used for this study. In Eq. (3), z_i represents the boundary layer height, computed in GEM following Seidel et al. (2012), T_v is the virtual temperature (computed here at the level closest to 10 hPa above the surface to reduce sensitivity to vertical resolution), θ_v it the virtual potential temperature, and standard Reynolds decomposition is implied by the division of the fields into turbulent (prime) and mean (overbar) components. The subscript "s" indicates that the term in parentheses in Eq. (3) represents the surface buoyancy flux, which is

[1] The free parameter c effectively acts as a threshold value because the cube root in Eq. (1) makes the value of δT_{vv} primarily sensitive to the sign of $w_g - c$ rather than the magnitude of the term.

positive in unstable conditions and negative when the surface layer is stable, as is the resulting estimate of w_*. The latter is an important scaling parameter for convective boundary layer thermals, and is directly related to the cloud base mass flux by Lock and Mailhot (2006). The estimates of c_{land} and c_{ocean} can be modified to adjust overall convective activity; however, their forms were established early in the development cycle and are considered fixed for the purposes of this study. For the adopted parameters, c tends to be larger over land than over ocean as shown in Fig. 2. This implies that convective initiation is favored over ocean compared to land for a given thermodynamic profile, a configuration that was found to yield the best overall precipitation structure during development.

The virtual temperature of the rising thermal determined through undilute parcel ascent and Eq. (1) is compared to the environmental virtual temperature at the LCL ($T_{v_{\mathrm{LCL}}}$). If the parcel is found to be negatively buoyant, then the trigger fails and the evaluation begins again for the next layer aloft until either an unstable parcel is found or the base of the departure level exceeds 300 hPa above the surface. If the parcel is positively buoyant at the LCL, then the trigger continues with an estimate of the updraft velocity of the thermal at the LCL:

$$w_{\mathrm{LCL}} = 1 + \sqrt{\frac{g\delta T_{vv}(z_{\mathrm{LCL}} - z_{\mathrm{USL}})}{4\left(T_{v_{\mathrm{USL}}} + T_{\mathrm{LCL}}\right)}}, \qquad (4)$$

where the "USL" subscript represents values taken from the lowest level of the updraft source layer. This approximation of the original Fritsch and Chappell (1980) formulation serves as the lower boundary condition for the integral used to compute the updraft velocity within the Kain and Fritsch (1990) plume model:

$$\Delta(w^u)^2 = \frac{2g\Delta z}{1+\lambda}\left(\frac{\overline{T_v^u} - \overline{T_v}}{\overline{T_v}} - D_p\right) - 2\varepsilon^u (w^u)^2, \qquad (5)$$

where g is gravitational acceleration, z is the height above ground, $\lambda = 0.5$ is an empirically derived constant, ε is the fractional entrainment rate, the superscript u indicates an updraft property, and overbars and Δ operators denote layer averages and finite differences, respectively. The D_p term in Eq. (5) represents the precipitation drag (Ogura and Cho 1973), and represents a small departure from the standard vertical acceleration model. As the lower boundary condition of Eq. (5), the estimate of w_{LCL} [Eq. (4)] therefore influences both the full updraft profile and the cloud top height, with the latter defined as the level at which w^u vanishes.

The influence of w_{LCL} on the updraft has a direct impact on the final component of the trigger, which confirms that the cloud depth exceeds a threshold value (3 km in the configuration used here). Updrafts that fail to meet this trigger condition typically occur in environments with large values of convective inhibition, wherein negative buoyancy above the LCL reduces the updraft velocity to zero before it can reach its level of free convection (Fritsch and Kain 1993). The larger the estimate of w_{LCL}, the greater the chances that the updraft will continue to rise through such a stable layer and grow into a deep convective cloud. It is the ability of this updraft property to represent an impulse sufficient to overcome convective inhibition that makes it an important quantity in this study.

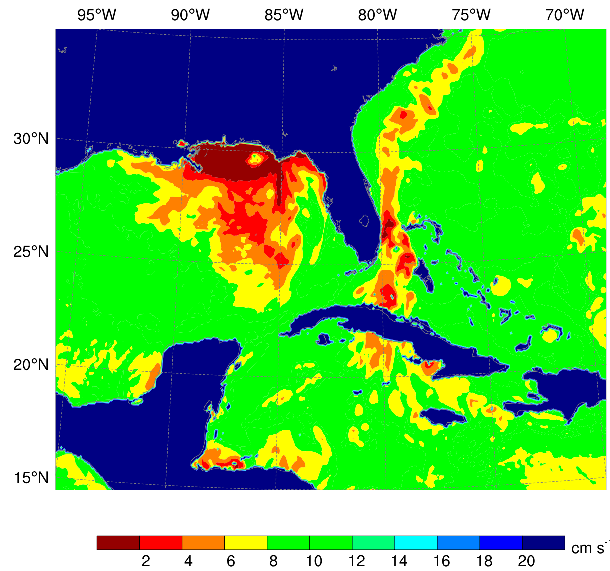

FIG. 2. Example of threshold vertical velocity (c; color shaded in 10^{-2} m s^{-1} as shown on the color bar) plotted over the subdomain of interest for section 3 at 1200 UTC 28 May 2018, after 24 h of model integration.

The cloud base updraft [Eq. (4)] links the trigger to the plume model, which computes entrainment and detrainment rates, and cloud properties (Kain and Fritsch 1990). This is followed by an estimate of evaporatively driven downdraft effects and a closure based on reduction of CAPE through the iterative solution of the mass flux equations. These aspects of the deep convective scheme used in GEM follow closely those described by Kain and Fritsch (1993) and will not be considered in more detail here.

c. Recent changes to the deep convective scheme

The position of the 10-km configuration used here at the upper end of the convective gray zone means that many of the underlying assumptions of the deep convection parameterization are potentially invalid. As a step toward relaxing some of these assumptions, one GEM development focus has been on improving the representation of convective structure and evolution by eliminating some of the quasi-equilibrium assumptions implicit in the scheme's configuration.

In the current deep convective scheme, CAPE is eliminated on a fixed time scale ($\tau_c = 2700\,\mathrm{s}$) once a grid cell becomes active. After initiation, convective tendencies, clouds and precipitation rates are held constant and none of the calculations described in the previous section are required over this period. The convective calculations can be refreshed more frequently using a second fixed time scale (τ_a), but in practice $\tau_c = \tau_a$ in most GEM configurations. Such a strategy is valid when the model time step is on the same order as τ_c; however, the 300 s step of the 10-km configuration implies that steady-state convection persists in place for nine time steps. To relax this constraint, convective calculations are refreshed at every time step ($\tau_a = 300\,\mathrm{s}$) in the updated scheme.[2]

Despite its conceptual appeal, however, the $\tau_a = 300\,\mathrm{s}$ configuration leads to intermittent triggering and unphysically short cloud lifetimes.[3] This is especially true in quasi-equilibrium cases (Zimmer et al. 2011) during which convective destabilization occurs on time scales similar to τ_c. Such a case was identified over the North Atlantic Ocean during development of the updated physics package (Fig. 3). The model represents such an equilibrium as stepwise activation and deactivation of the convective scheme. This unphysical behavior is indicative of a lack of memory in the system as described by Gerard et al. (2009). In sections 4 and 5, a pair of independent strategies are developed to avoid such problems by adding memory to a deep convection parameterization in a Lagrangian framework.

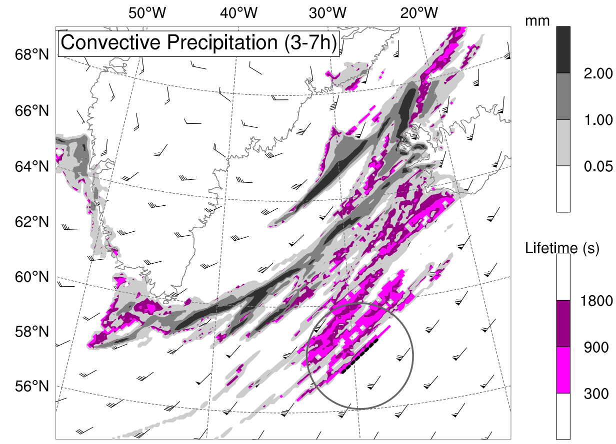

FIG. 3. Convective precipitation accumulations between 3 and 7 h of forecast lead time in an integration initialized at 0000 UTC 16 Jan 2017 (gray shaded in mm as shown on the upper grayscale bar), and mean lifetime of convective activity at each grid cell over the period (magenta shaded in seconds as shown on the lower color bar, overlaid on the precipitation field). In this simulation, $\tau_a = 300\,\mathrm{s}$ is used, such that convective calculations are updated at every time step. Also shown are the mean free-tropospheric winds (850–200 hPa layer average), represented as wind barbs with short, long, and pennant barbs representing 5, 10, and 25 m s^{-1} wind speeds, respectively). The flow-aligned section used to illustrate the evolution of convection in Fig. 18 is shown with a black dashed line within a larger gray circle for ease of reference.

3. Tropical precipitation case study: Tropical Storm Alberto (2018)

The static nature of the triggering and maintenance of parameterized deep convection leads to problems with predicted precipitation that are most evident under large-scale high-wind conditions in the tropics. In such an environment, convective clouds can move over long distances while being sustained by readily available moisture and warm sea surface temperatures (Hennon et al. 2013). The Caribbean Sea and Gulf of Mexico represent an ideal laboratory for studies of complex convective structures because of the prevalence of coastlines and islands of varying sizes (Kirshbaum and Smith 2009).

Tropical Storm Alberto (2018) formed beneath an upper-level trough along the east coast of the Yucatan Peninsula on 25 May 2018 from a larger low that had persisted in the region for several days (Berg 2018). As a result of the extratropical features that promoted its development, Alberto maintained the asymmetric structure of a subtropical storm (Evans and Guishard 2009; da Rocha et al. 2019) as it moved northward into the Gulf of Mexico on 26 May (Fig. 4). Heavy precipitation that formed in the extensive cloud shield to the east of the storm caused severe flooding and triggered landslides in Cuba that killed 10 people. Alberto intensified steadily as it underwent tropical transition (Davis and Bosart 2004) on 27 May and became a tropical storm at 0000 UTC 28 May to the west of Florida with estimated peak winds of 55 kt (1 kt ≈ 0.5144 m s^{-1}). Despite its tropical designation, strong large-scale southerly flow persisted to the east of the storm throughout this period, bringing heavy rains to Cuba and the Bahamas. Alberto weakened prior

[2] Because only a small fraction of grid points pass the convective trigger tests (~5% of the domain in the summer) and the deep convection scheme accounts for <5% of the computational cost of model physics, the adoption of stepwise refreshment does not add significantly to the time-to-solution of the system.

[3] A cloud lifetime is computed in the traditional parameterization framework as the length of time that convection remains active within a grid cell. It is deemed to be unphysical if it is shorter than the time required to initiate, build, and decay a deep convective cloud: ~1800 s is proposed by Houze (1994).

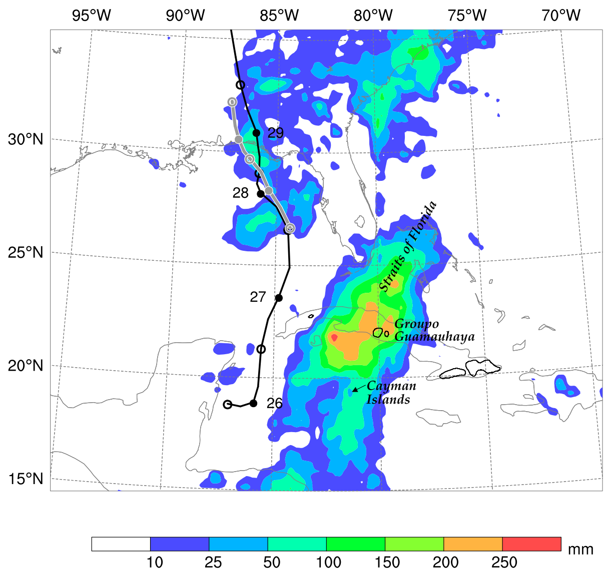

FIG. 4. Track of Tropical Storm Alberto [black line with filled dots for 0000 UTC positions, open dots for 1200 UTC positions, and ordinals for dates in May 2018 following the best track of Berg (2018)] and 24-h precipitation accumulation estimates (0000 UTC 28 May–0000 UTC 29 May) from the Tropical Rainfall Measuring Mission [Goddard Earth Sciences Data and Information Services Center (2016); color shaded in mm as shown on the color bar]. Alberto's track in the GEM control integration is shown in gray, with dots representing synoptic hours as for the best track. The 200 m contour of Cuban orography is shown with a black contour, and locations discussed in the text are labeled for reference.

to making landfall on the Florida Panhandle at 2100 UTC 28 May, but was still capable of generating flooding rains as it continued northward to eventually dissipate near the Great Lakes on 31 May (Berg 2018).

The 48 h simulations shown in this study are initialized from the Canadian regional analysis at 1200 UTC 27 May, shortly before Alberto became a tropical storm. Rainfall in Cuba peaks on 28 May, with 24 h accumulations ending at 0000 UTC 29 May estimated by the Tropical Rainfall Measuring Mission to exceed 250 mm (Fig. 4). Precipitation accumulations along the U.S. Gulf Coast surpass 50 mm over the same period. The control GEM integration depicts Alberto's track with sufficient skill for the purposes of this investigation. More importantly, the model reproduces the strong southerly flow that develops between the storm and the mid-Atlantic subtropical high, and the associated axis of maximum rainfall that extends from the Cayman Islands into the Straits of Florida (Figs. 4 and 5a).

Despite the model's success in reproducing the general precipitation structure in this case, two notable problems appear in Figs. 5a and 5b. The first is that accumulations are underpredicted over Cuba by about 50 mm, and overpredicted downstream to the west of the Bahamas. The second problem is directly related to land–sea contrasts: rainfall over Cuba is reduced with respect to the surrounding waters. Similarly, there is an abrupt reduction in rainfall along the Gulf Coast, particularly at the eastern end of the Florida Panhandle. Although the deep convective scheme contributes to only about 50% of total rainfall over this period, the bulk of these coastal discontinuities appears to stem from convective accumulations (Figs. 5c,d). Identifying the source and addressing the root cause of these unphysical patterns are the goals of sections 4 and 5 of this study.

4. A Lagrangian view of convective initiation

The coastal discontinuities in convective precipitation accumulation (Figs. 5c,d) align with those noted for the threshold vertical velocity (c) in section 2b (Fig. 2). Given the strong dependence of the activity of the deep convective scheme on c, it is likely that the sharp precipitation gradients are more related to the trigger function than to abrupt changes in the atmospheric state that stabilize profiles at the coast.

The direct relationship between c and the temperature perturbations of thermals rising from the PBL [Eq. (1)] suggest the source of the problem. Such motions have intrinsic time scales on the order of those of the PBL itself, especially when an ensemble of thermals that might trigger moist convection anywhere within a grid cell is considered instead of a single updraft in isolation. The characteristics of such thermals are properties of the PBL air parcel that are not uniquely specified by the type of surface over which the parcel currently resides as implied by Eq. (2).

The recognition of c as an air parcel property related to thermal perturbations with sources based on local conditions suggests that it would be well represented as an advected field with Newtonian relaxation (c_{adv}). This can be formulated as an equation for the local c_{adv} tendency that has the following form:

$$\frac{\partial c_{\mathrm{adv}}}{\partial t} = -\mathbf{V} \cdot \nabla c_{\mathrm{adv}} + \frac{1}{\tau_{\mathrm{therm}}}(c - c_{\mathrm{adv}}), \tag{6}$$

where $\mathbf{V}$ is the three-dimensional wind vector and τ_{therm} is a relaxation time scale for thermal activity in the parcel. The model is initialized with $c_{\mathrm{adv}} = c$ at all levels (initially vertically uniform), which then evolves following Eq. (6), with c_{adv} treated as a tracer quantity by the model's semi-Lagrangian advection scheme. The value of $c(\mathbf{X}, t)$ employed in Eq. (1) is diagnosed at the LCL using the same linear vertical interpolation as applied to all other gridscale quantities. A relaxation time scale of $\tau_{\mathrm{therm}} = 3600$ s is adopted for consistency

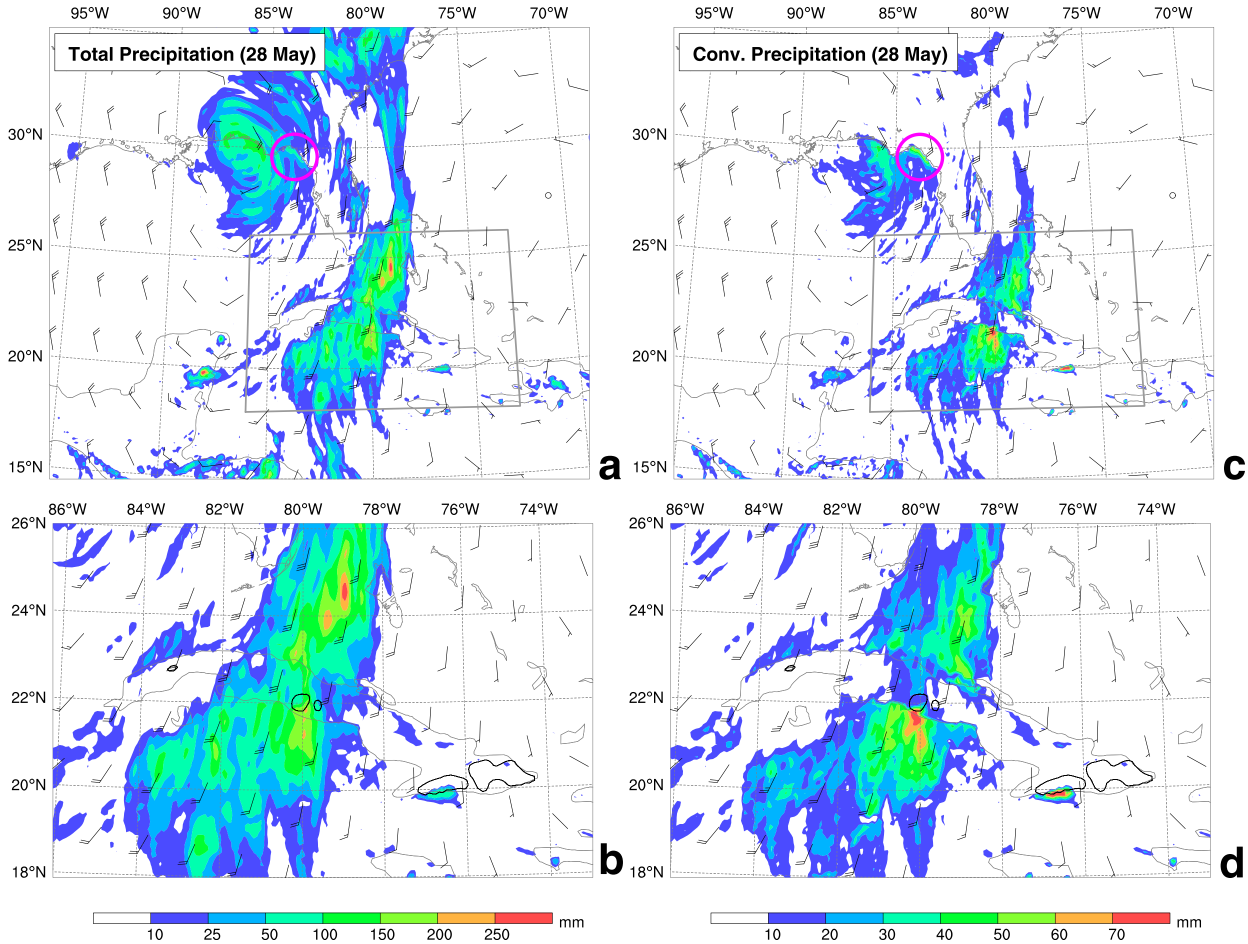

FIG. 5. Accumulation of 28 May precipitation in the control simulation (color shaded in mm as shown on the color bars, which are different for the two columns), and daily average 850–200 hPa layer-mean winds (wind barbs plotted as in Fig. 3). (a),(b) Total accumulated precipitation and (c),(d) the contribution from the deep convection scheme are shown. (top) A regional view of the fields, and (bottom) zoomed-in view centered on Cuba as shown with gray outlines shown in (a) and (c). Precipitation discontinuities along the U.S. Gulf Coast are highlighted in (a),(b) with magenta circles. The 200 m contour of Cuban orography seen by the model is shown in (b),(d) with a black contour.

with the duration of convective memory in the subcloud thermodynamic profile (Colin et al. 2019).

The resulting c_{adv} field is free of abrupt coastal discontinuities and has larger spatial scales than the original estimate of c (cf. Figs. 2 and 6), consistent with the Kain (2004) interpretation of the Eq. (1) factors as environmental conditions rather than gridpoint values. Small changes to τ_{therm} do not qualitatively affect the results shown here, but in the limit of rapid adjustment of parcel properties ($\tau_{\mathrm{therm}} \rightarrow 0$ s), an implicit solution for Eq. (6) ensures that $c_{\mathrm{adv}} = c$ such that the Lagrangian treatment of the thermal updrafts disappears.

This Lagrangian treatment of the properties of the thermals within the parcel that may trigger moist convection reduces the magnitude of the coastal discontinuities in convective precipitation (cf. Figs. 5c,d and 7c,d, with difference shown in Fig. 8). This is true not only along the windward coastlines of Cuba and Florida, but also in the lee of Cuba, where oceanic convection spins up gradually offshore rather than triggering immediately along the coastline.

Despite these improvements in the convective rainfall pattern from a physical perspective, increased convective activity does not extend across Cuba (Fig. 8b), which remains a local convective rainfall accumulation minimum (Fig. 7d). Although some windward enhancement and rain shadowing by the Groupo Guamauhaya mountain range of central Cuba (elevations up to 1100 m; see Fig. 4 for reference) is expected, convective activity over the island remains unrealistically weak in this integration (Fig. 7).

One reason for suppressed convective activity over land in the model appears to be a near-surface stable layer that remains in place over the western and central

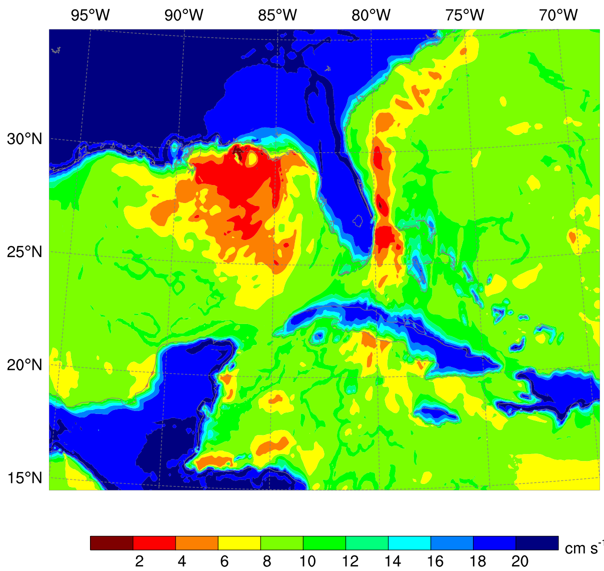

FIG. 6. As in Fig. 2, but for c_{adv} [Eq. (6)] rather than c [Eq. (2)].

Cuba throughout 28 May. Dense upper-level cloud cover prevents daytime warming over the island, leading to near-surface temperatures that are 5 K cooler than the surrounding ocean (Fig. 9). The early afternoon model soundings around Santa Clara show that this stable layer extends to 900 hPa, above which the profile is conditionally unstable (Fig. 10). Air parcels rising from the surface encounter large convective inhibition within the capping inversion, such that no realistic temperature perturbation in surface-based thermals (δT_{vv}) is expected to trigger parameterized convection.

Initiation of convection by parcels originating above 900 hPa appears to be possible in the Santa Clara profile (Fig. 10); however, such elevated triggering would require a positive δT_{vv} of 1–2 K to overcome convective inhibition. Such a positive δT_{vv} requires $w_g > c(\mathbf{X}, t)$, where $c(\mathbf{X}, t) \geq 0.02\,\mathrm{m\,s^{-1}}$ [Eq. (1)]. This condition is clearly not met, as downward resolved mass fluxes (ρw_g, where ρ is the air density) dominate over Cuba (Fig. 11).

The subsidence over the island (Fig. 11) arises from two sources: a thermal circulation that is maintained by the land–sea temperature difference (Fig. 9), and a mountain-wave response to the local orography. The former is the result of differential lower-level heating, which preferentially creates potential instability over the waters surrounding Cuba. Ascent in these regions is fueled by latent heat release at the grid scale, with the 300 hPa outflow layer leading to convergence and upper-tropospheric subsidence that further stabilizes the Cuban profile. In the lower troposphere, a mountain wave that is triggered by the southerly large-scale flow drives subsidence despite the modest terrain height. An experiment run without Cuban orography shows that a lower-level thermal circulation maintains weak subsidence even in the absence of the mountain wave, with vertical motion values well below those required to create a positive δT_{vv} for convective triggering (not shown).

The fact that cloud formation in both the gridscale condensation scheme and convection parameterization is strongly dependent on w_g means that the model becomes locked into a thermally direct circulation in response to the stationary surface forcing under steady flow conditions. In the absence of local initiation [$w_g < c(\mathbf{X}, t) \rightarrow \delta T_{vv} < 0$], any convection that occurs inland over Cuba must be triggered over the water and transported across the island by the strong southerly flow. The importance of such deep convective cloud displacement is assessed in the next section of this study.

5. An object-based framework for deep convective clouds

The dearth of convective activity over Cuba that persists despite the use of Lagrangian initiation can be interpreted as the failure of the model to represent the displacement of convective clouds in a physically reasonable way. A convective cell that forms immediately upstream of Cuba may progress inland a significant distance before decaying, despite the presence of the stable near-surface layer described in the previous section. Soderholm et al. (2014) show that isolated cells can survive in hostile environments (with high values of convective inhibition) particularly under conditions of strong lower-level shear and background winds. They attribute such a life cycle to enhanced organization of the cloud structure that leads to stronger internal dynamical forcing in environments with a low bulk Richardson number (Weisman and Klemp 1982). The latter is defined as

$$R_b = \frac{\mathrm{CAPE}}{0.5|\Delta U|^2}, \tag{7}$$

where CAPE is the convective available potential energy and ΔU is the magnitude of the bulk 0–6 km wind shear. In the case considered here, $13\,\mathrm{m\,s^{-1}}$ of shear over this layer combines with the low CAPE values in the profile (approximately $500\,\mathrm{J\,kg^{-1}}$ for a parcel lifted from 900 hPa in the model Santa Clara sounding shown in Fig. 10) to yield $R_b \approx 6$, sufficient to promote the maintenance of long-duration, long-track convective elements (Soderholm et al. 2014).

Despite the introduction of Lagrangian initiation (section 4), the deep convection scheme has a limited

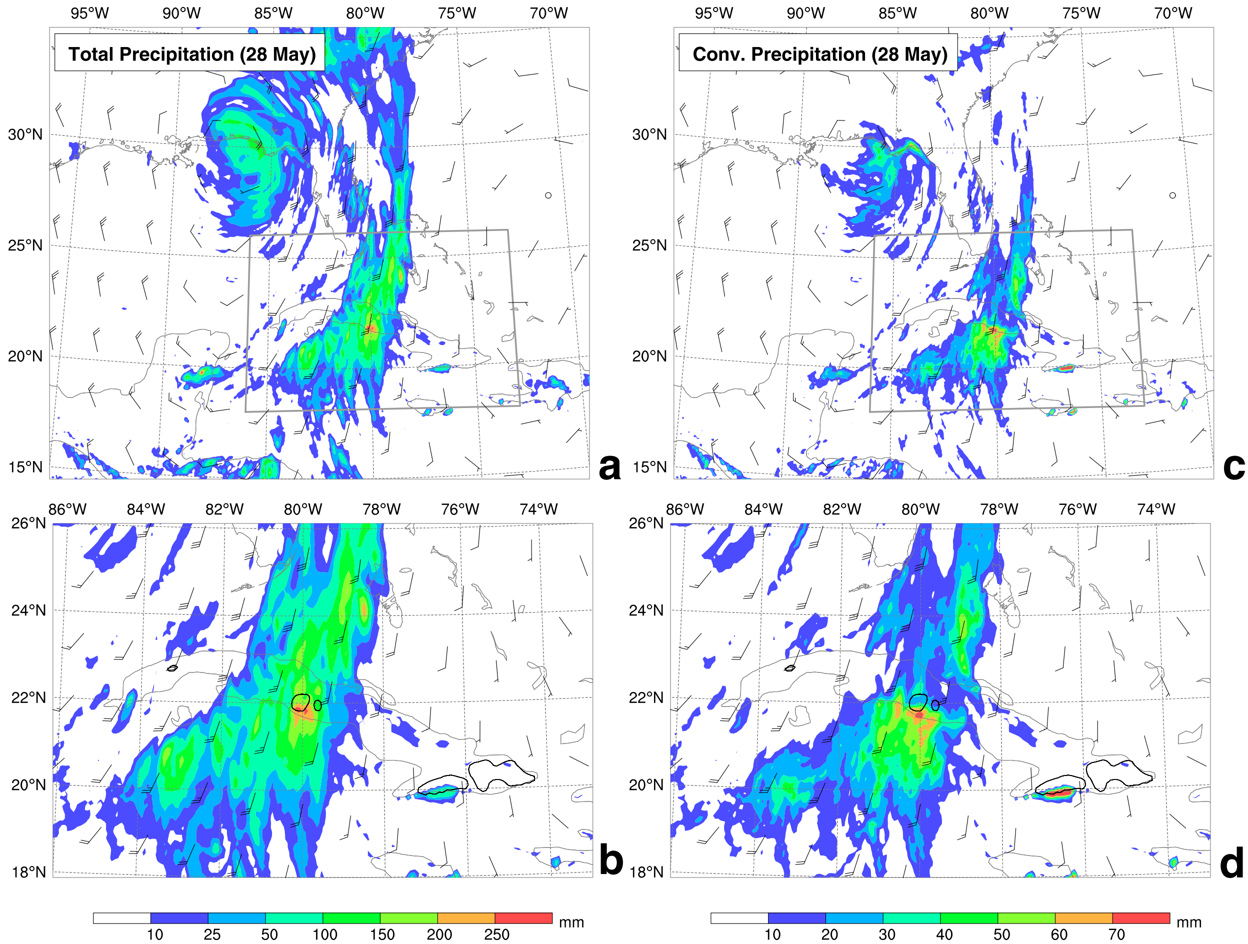

FIG. 7. As in Fig. 5, but for an integration that takes a Lagrangian view of convective initiation by using c_{adv} [Eq. (6)] rather than c [Eq. (2)].

ability to represent the maintenance and displacement of convective cells in such an environment because of the static nature of convection parameterization described in sections 2b and 2c. Such a framework was justified in the models for which schemes such as Kain and Fritsch (1990) were developed, with large horizontal grid spacings and time steps. In such systems, the effects of clusters comprising numerous convective elements were parameterized on time scales that approached those of the cloud ensemble itself (Zimmer et al. 2011). However, as model resolution approaches the convective gray zone and time steps are reduced well below those of even individual convective clouds, the validity of a stationary, equilibrium treatment of parameterized convection becomes questionable.

a. *Description of an object-based scheme*

One solution to the inconsistencies that emerge as resolution approaches the gray zone may lie in an "object-based" view of deep convective clouds (Fig. 12), a term borrowed from the object oriented paradigm of computer science around which it is structured. In this framework, clouds are considered to be persistent entities with properties that evolve throughout their life cycles. Readers familiar with object-oriented design can conceptualize individual cloud objects to be instances of a convective cloud class, each possessing its own attributes that are modified by methods defined in the parameterization. This approach allows convective clouds to evolve in space and time in a physically realistic manner that is more consistent with gray zone resolutions.

The formation of a new cloud object follows the Lagrangian convective initiation described in section 4. Once convective activity is confirmed by the trigger, however, additional actions are needed to set initial cloud attributes (Fig. 13 and Table 1). In the current implementation, the new cloud is positioned at the center of the grid cell (randomized subgrid positioning was not found to yield any benefit in the deterministic system considered here), the cloud age (t_{co}) is set to the model time step, and the cloud base updraft speed (w_{LCL}) is computed following Eq. (4) for the initiation branch of the trigger.

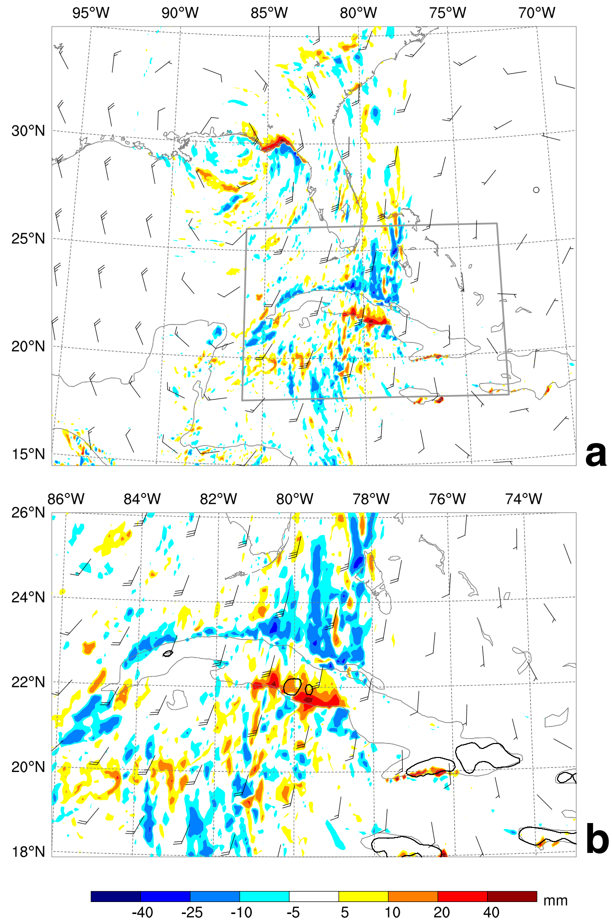

FIG. 8. Difference in convective precipitation accumulation on 28 May between an integration that takes a Lagrangian view of convective initiation (as in Figs. 7c,d) and the control (as in Figs. 5c,d). Plotting of orography, wind field, and zoomed region follows Fig. 5.

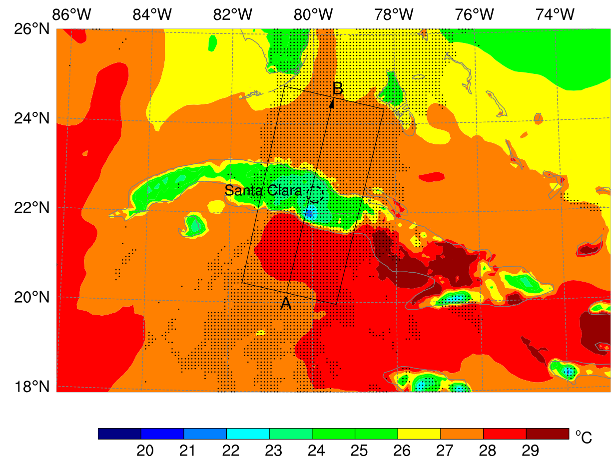

FIG. 9. Mean screen-level temperature on 28 May in the control integration (color shaded in °C as shown on the color bar). Black stippling indicates areas over which the mean cloud cover during the integration exceeds six octas (75%). The region surrounding Santa Clara is identified with a dashed circle for reference with the text and Fig. 10. A black polygon outlines the region used for the cross-sectional average shown in Fig. 11, which is centered on the A–B vector.

The movement of the convective cloud object is governed by the cloud layer-mean winds:

$$(x_{\rm co}, y_{\rm co}) = (x_{\rm co}, y_{\rm co})_\circ + \frac{\int_{z_b}^{z_t} \mathbf{V} dz}{\int_{z_b}^{z_t} dz}\Delta t, \quad (8)$$

where ($x_{\rm co}$, $y_{\rm co}$) is the cloud position [with a subscript "$\circ$" for the position at the beginning of the time step (Δt)], $\mathbf{V}$ is the horizontal wind, z is height above ground, and z_t and z_b are the cloud top and base heights, respectively. This formulation of cloud motion corresponds to the advection of individual mesobeta-scale convective elements described by Corfidi et al. (1996). The propagation mechanisms associated with mesoscale convective complexes are not currently considered in cloud object displacement. However, this dependency on the model's ability to resolve the processes that occur at these larger scales of organization is a design decision for the current implementation rather than a fundamental limitation of the approach. The fact that ($x_{\rm co}$, $y_{\rm co}$) in Eq. (8) are positions in physical space (Table 1) gives the cloud object permanence that is independent of the model grid. This means that the cloud moves downstream in a continuous fashion through advection by the resolved flow.

Once a preexisting cloud object is detected within a grid cell, a second branch of the convective trigger is activated (Fig. 13). This new branch is associated with preexisting convection (either present within the grid cell at the previous time step or transported from an upstream location), and makes direct use of the $w_{\rm LCL}$ of the cloud object. The standard initiation branch of the trigger is also executed at the grid cell, representing the potential formation of new convective clouds within the same volume by thermal activity in the boundary layer. The maximum estimate of $w_{\rm LCL}$ from these two branches is used as the basis for the subsequent plume model calculations because it is the most likely to yield clouds deep enough to perpetuate convective activity in the grid cell. If the initiation-branch $w_{\rm LCL}$ estimate is selected, then the cloud object properties are reset to their initial values (Table 1) to represent the development of a new convective cloud. If the preexisting updraft estimate is dominant, then the object properties are updated as described in the final column of Table 1 and the cloud continues to drift downstream.

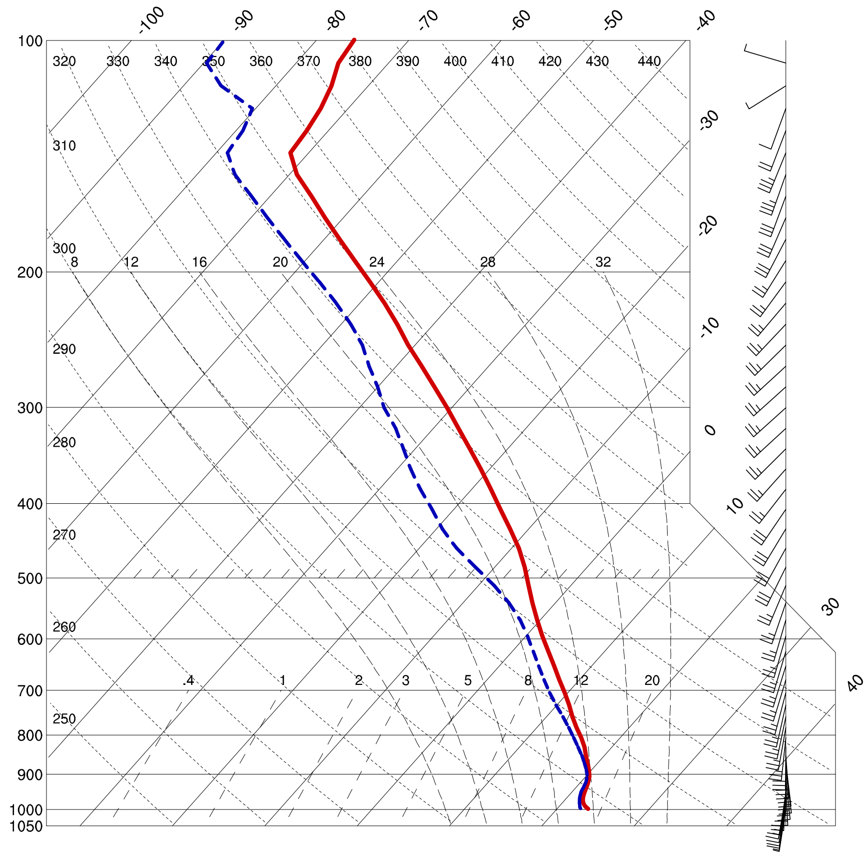

FIG. 10. Model sounding for the Santa Clara region, valid at 1800 UTC 28 May 2018 (1300 h local time) after 30 h of integration. The dry bulb temperature is shown with a solid red line, the dewpoint temperature with a dashed blue line, and winds are plotted with barbs as described in the Fig. 5 caption. The sounding is an average of all nonconvective points within a 20 km radius of Santa Clara, Cuba, as shown with the dashed circle in Fig. 9.

In the event of confluent flow, multiple cloud objects can be diagnosed within a single grid cell. In this case, the cloud with the strongest w_{LCL} is selected to continue its life cycle so long this value exceeds the initiation branch estimate. The rationale for this choice mirrors that of the selection between preexisting and initiation updrafts described above, in that the cloud with the largest updraft speed is the most likely to maintain itself at subsequent time steps.

With the addition of a triggering branch for preexisting convection, the estimate of w_{LCL} takes on increased importance. Not only is the value used to initiate the convective plume, but also it becomes a key ingredient for determining the longevity of convective cloud objects and therefore convective activity more generally. Because w_{LCL} is a property of the cloud model rather than the closure, it is not modified by the convective scheme after its initial estimate in the trigger function. If nothing were done to impose a reduction of the w_{LCL} cloud object property over time, this value would not evolve until the existing cloud was either replaced by new convective initiation or found to unable to sustain convective activity. In this study, we set a time scale of $\tau_{\mathrm{co}} = 3600\,\mathrm{s}$ and impose exponential decay through

$$w_{\mathrm{LCL}}(t_{\mathrm{co}}) = w_{\mathrm{LCL}_i} e^{-t_{\mathrm{co}}/\tau_{\mathrm{co}}}, \tag{9}$$

where w_{LCL_i} is the estimate of w_{LCL} computed by Eq. (4) at convective initiation. This time scale is consistent with existing estimates of the convective life cycle (Bullock et al. 2015) and the convective memory diagnosed by Colin et al. (2019). A more physically based representation of updraft evolution would involve the introduction of a prognostic updraft equation as proposed by Gerard and Geleyn (2005); such an improvement in the representation of the updraft evolution during the cloud life cycle will be the subject of future investigation. In the short time-scale limit ($\tau_{\mathrm{co}} \rightarrow 0$) the trigger branch for preexisting convection becomes

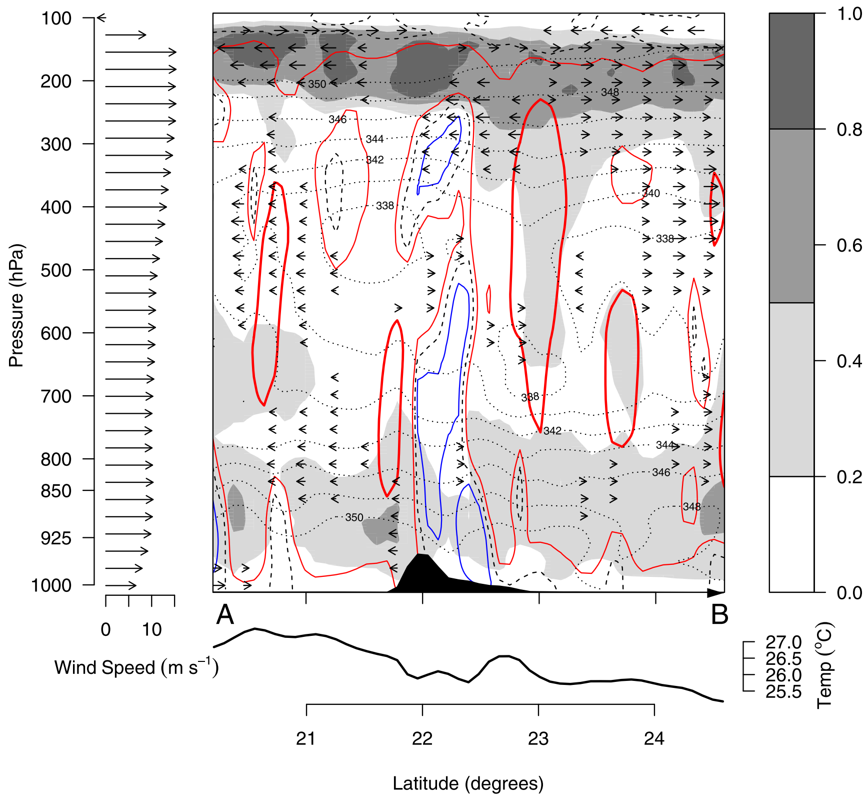

FIG. 11. Streamwise cross section of cloud fraction (gray shaded as shown on the grayscale bar), resolved mass flux (solid blue contours for downward, solid red for upward, and dashed black for 0 kg m^{-2} s^{-1}, with absolute values of 0.015 kg m^{-2} s^{-1} and 0.1 kg m^{-2} s^{-1} shown with thin and thick lines, respectively), equivalent potential temperature (black dotted lines at 2 K intervals), and anomaly streamwise wind (plotted only for wind speeds >1 m s^{-1}, using the same vector scale as the abscissa of the left panel). The mean wind profile is shown to the left of the main panel, and the mean screen-level air temperature is shown below the main panel. All fields are valid at 1800 UTC 28 May 2018 and averaged across the A–B flow over the region identified with a black box in Fig. 9.

increasingly unviable and the scheme returns to the conventional initiation-only convective parameterization of Fig. 1.

b. Impact on the tropical precipitation case study

The adoption of a cloud object-based perspective for the Tropical Storm Alberto case study is expected to assist with the realistic maintenance of convection as clouds encounter near-surface stability over Cuba (Fig. 10). The strong southerly flow advects cloud objects rapidly inland, where they can continue to promote convection despite a lack of new initiation by rising thermals.

As shown in Fig. 14d, convective accumulations in excess of 20–30 mm now cross the island near the Groupo Guamauhaya mountain range. Precipitation enhancement associated with this orographic feature is shifted slightly farther inland, and a realistic rain shadow is evident downstream (Fig. 15b). Increased convective rainfall accumulations are no longer restricted to the coastal region as they were when Lagrangian initiation was adopted in isolation, but instead extend across the Cuban landmass (cf. Figs. 8b and 15b). Although the near-surface stability precludes the triggering of new convection, convective activity persists as cloud objects cross the island (Fig. 16b). A deep convective cloud traveling with the 25 to 30 kt mean tropospheric flow would take approximately 2 h to cross the 100 km width of the island. This suggests that the most vigorous convective elements are able to transit Cuba without dissipating in this integration provided that the local environment does not become hostile enough to suppress even preexisting updrafts (warm-colored shading in Fig. 16b).

At the larger scale, the increased convective activity over Cuba appears to deplete moisture in the southerly flow sufficiently to reduce the precipitation maximum downstream of the island that plagued the control

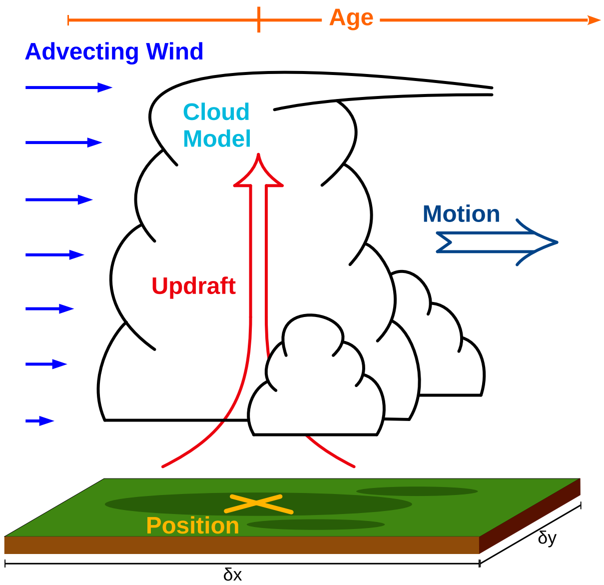

FIG. 12. Schematic view of a deep convective cloud object within a grid cell, with annotations for object properties (attributes; warm colors) and process depictions (methods; cold colors) of particular interest in this study.

integration (cf. Figs. 5a and 14a). The net result is a regional accumulated precipitation structure that more closely resembles corresponding observational estimates (Fig. 4).

Changes in precipitation structure are not limited to the Cuban region. Accumulations also extend farther inland over the Gulf Coast (Fig. 15a), again reflecting the persistence of preexisting convective activity as it moves into an environment that is less supportive of convective initiation. The convective cells age in a physically reasonable manner as they move across the Florida Panhandle, as they do in Alberto's rainbands over the Gulf of Mexico (Fig. 16a).

6. Impact of changes on NWP guidance

The Tropical Storm Alberto case study considered in sections 4 and 5 represents a relatively extreme example of extensive convection in a strong large-scale flow. As such, it is useful for assessing the physical relevance of the Lagrangian view of deep convection and for establishing an upper bound on the impact of this framework on large-scale precipitation structure. Here, we consider the effect of the Lagrangian treatment in less extreme cases and on objective precipitation scores more generally.

a. *Cloud and precipitation structures*

1) SUMMER SQUALL-LINE CASE

Included in the two-month summer test period (mid-June to mid-August 2016) used during development of the Regional Deterministic Prediction System is a case that highlights the impacts of model changes on a severe weather outbreak in the midwestern United States. A mesoscale convective system located over central Minnesota at the model initialization time (0000 UTC 5 July 2016) combines with isolated convection over Iowa to form a squall line that propagates southeastward overnight into Illinois by 1400 UTC (0800h local time; Fig. 17).

The operational configuration of the model fails to generate a coherent squall line, and instead predicts scattered cells displaced to the south of the observed feature (Fig. 17b). When the full Lagrangian treatment of deep convection is applied (sections 4 and 5), the precipitation pattern is more spatially coherent, with envelope that centers on the observed squall line location[4] (Fig. 17c). The impact of the Lagrangian treatment of convective clouds is even more striking after sunrise, with the isolated cells of the control integration transformed into a bowing line as in the radar precipitation estimate (Figs. 17d–f). Such an enhancement of convective organization is consistent with the introduction of additional convective-scale memory in the system (Davies et al. 2013). In this case, the change in structure is uniquely related to the introduction of cloud objects because $c = c_{\mathrm{land}}$ for such continental regions. Although there is little surface precipitation in the trailing stratiform region in either configuration, the overall structure of the squall line appears to be better represented in the integration using the Lagrangian framework.

2) INTERMITTENT TRIGGERING IN A MARGINAL ENVIRONMENT

Problems with precipitation structure in more mundane precipitation events include the intermittent activation of the deep convective scheme (section 2c and Fig. 3). The stream-wise life cycle of deep convective activity in a low-CAPE environment is shown in Fig. 18. In the operational system, the convection scheme remains active at a triggered grid point over a specified adjustment time scale (Bechtold et al. 2008). This leads to isolated cells that remain stationary despite the $13\,\mathrm{m\,s^{-1}}$ mean flow (Fig. 18a). Although such stationary features are sometimes observed in "back-building" convection, they are clearly unphysical in a scheme that does not represent such internal storm dynamics.

[4] The results shown in Fig. 17 are robust to both initial condition and convective time-scale perturbations, suggesting that differences are physically robust and not a result of "chaos seeding" (Ancell et al. 2018).

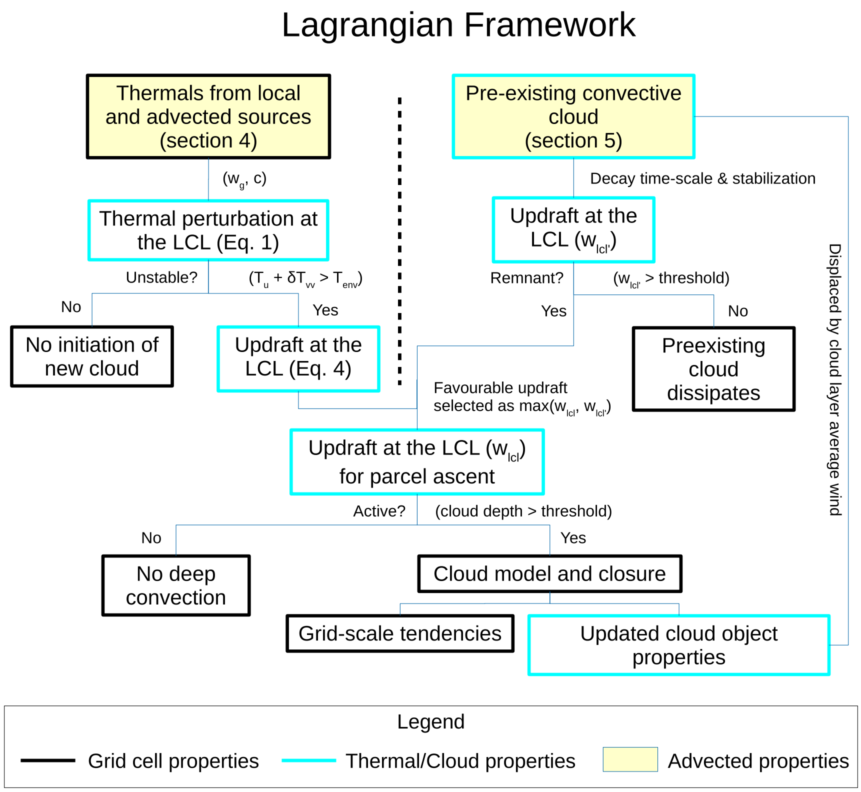

FIG. 13. Schematic of the convective scheme with Lagrangian initiation and convective cloud objects.

With convection calculations refreshed on every time step (section 2c), convection is triggered at successive positions downstream, giving the appearance of more realistic cell motion despite the fact that there is no explicit displacement (Fig. 18b). The intermittency problem that plagues this configuration (Fig. 3) is evident in the discontinuous downstream triggering and short convective lifetimes in this configuration (section 2c).

When the Lagrangian framework is adopted, cloud objects age as they are advected downstream (Fig. 18c). The two primary clouds on this transect each move approximately 100 km (10 grid lengths) over their 2-h life cycles. This convective behavior is much closer to reality than that of the existing configurations. The proposed framework therefore appears to be capable of reducing the prevalence of convective precipitation structure artifacts that affect the day-to-day guidance produced by the GEM model.

b. *Objective scores*

The focus of this study has been on improving the physical foundations of one aspect of convection parameterization (convective memory as represented by the evolution and displacement of clouds and updrafts) that is problematic at resolutions approaching the convective gray zone. Its goal is not to achieve general improvements in objective precipitation scores, but rather to make qualitative improvements in precipitation structure guidance (Davies et al. 2009). Although the two are certainly related (improved predictions of precipitation structure should improve objective scores), the convection parameterization is active at such a small

TABLE 1. Description of deep convective cloud object properties (shown in warm colors in Fig. 12). All symbols are described in the text with the exception of $t_{co_\circ}$, which is the cloud object age at the beginning of the time step.

Property	Description	Symbol	Initialization	Evolution
Position	Latitude and longitude of the cloud object	(x_{co}, y_{co})	Center of grid cell	Eq. (8)
Updraft	Updraft at the LCL	w_{LCL}	Value diagnosed by Eq. (4)	Eq. (9)
Age	Age of the cloud object	t_{co}	Δt	$t_{co} = t_{co_\circ} + \Delta t$

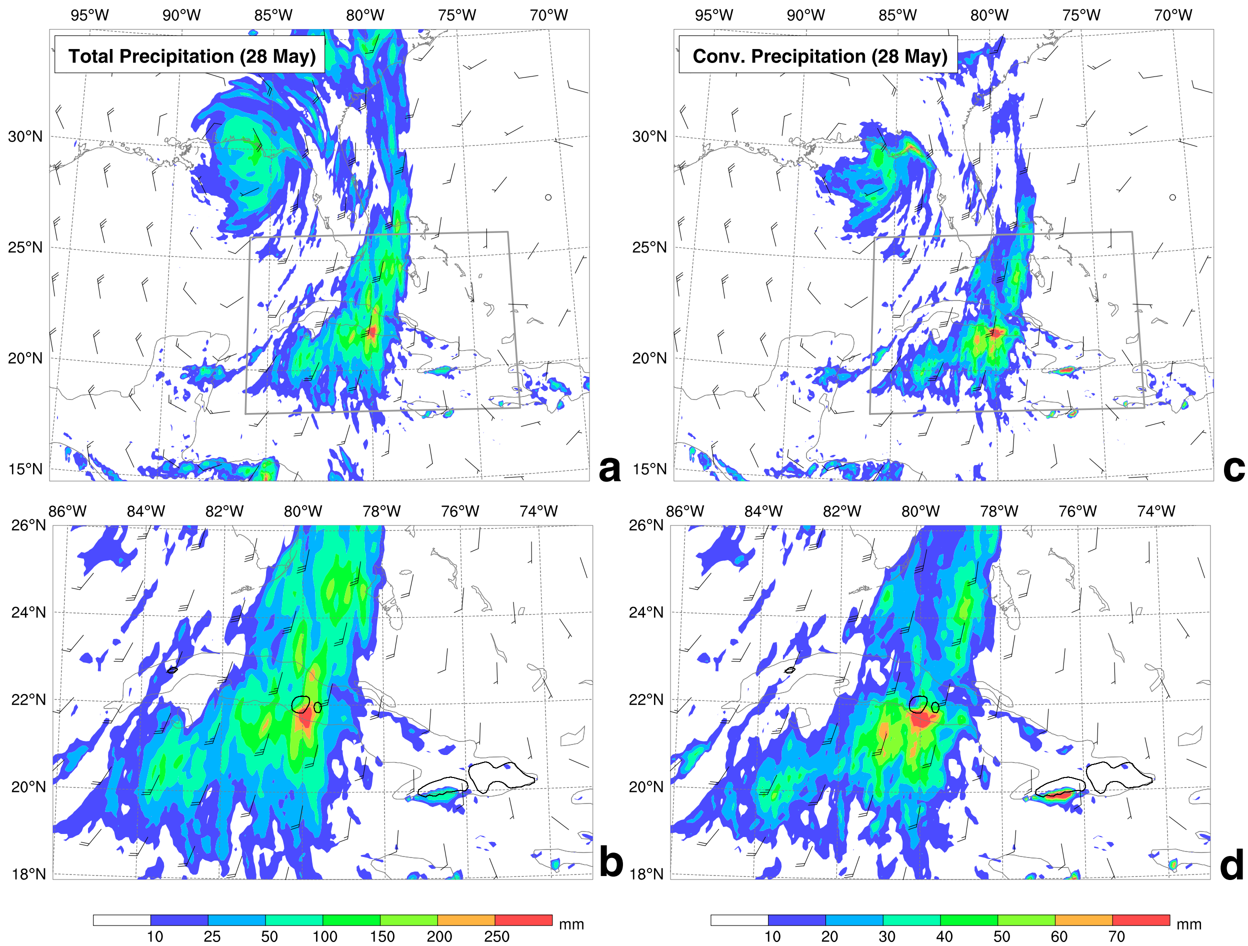

FIG. 14. As in Fig. 7, but for with the addition of deep convective cloud objects.

fraction of grid points in a typical integration with a 10-km model (<5%), that generalized precipitation score improvements are unlikely.

A set of 44 summer-2016 integrations are used for objective evaluation during GEM development, spaced at 36 h intervals to promote serial independence. This dataset is split into a pair of 22-case subsamples based on initialization time, with only the 1200 UTC initializations considered here. The impact of adopting a Lagrangian view of deep convection in this context is shown in Fig. 19. The equitable threat score is improved for all precipitation thresholds, although the difference is statistically significant only when accumulations surpass 2 mm 24 h^{-1} (Fig. 19a). A general increase in rainfall leads to a positive frequency bias at most thresholds (Fig. 19b), a reflection of a reduction in the number of missed events. The latter is demonstrated by the unchanged false alarm ratio (Fig. 19d), combined with an improved probability of detection (Fig. 19c), particularly at the lower thresholds where the convection parameterization contributes most significantly to rainfall totals. These results provide evidence that the scheme is generally working in a physically realistic manner when the Lagrangian perspective is adopted.

7. Discussion

The parameterization of moist convection as a subgrid-scale process continues to be essential to NWP, even as finer grid spacings take operational models well into the convective gray zone. However, many of the fundamental assumptions upon which these schemes are based become increasingly invalid as convection becomes partially resolved. The goal of this study has been to address one aspect of this problem that leads directly to logical inconsistencies that appear as model temporal and spatial scales become comparable to those of the cloud life cycle. The approach described here involves the development of a Lagrangian framework for the treatment of both convective initiation and deep cumulus clouds themselves.

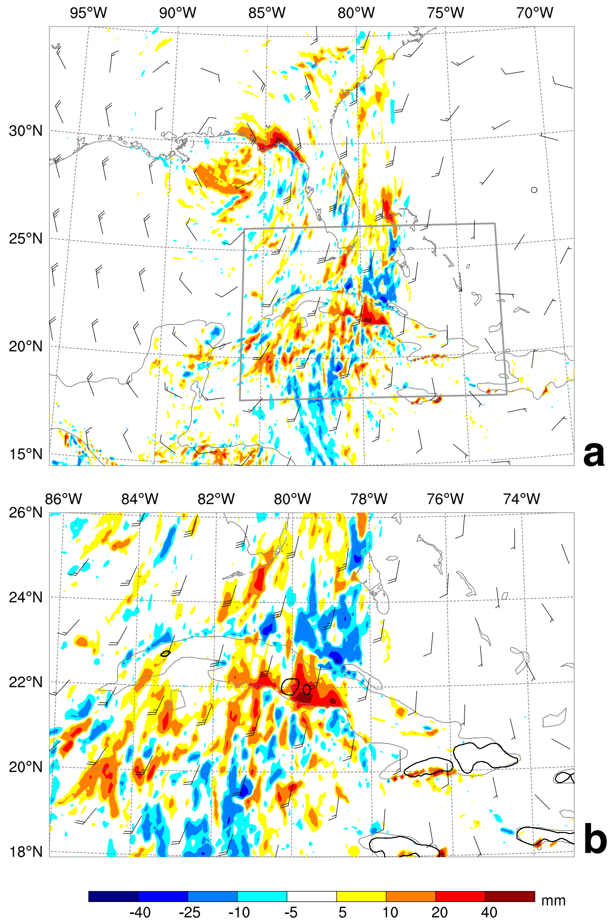

FIG. 15. As in Fig. 8, but with the addition of deep convective cloud objects as in Figs. 14c and 14d.

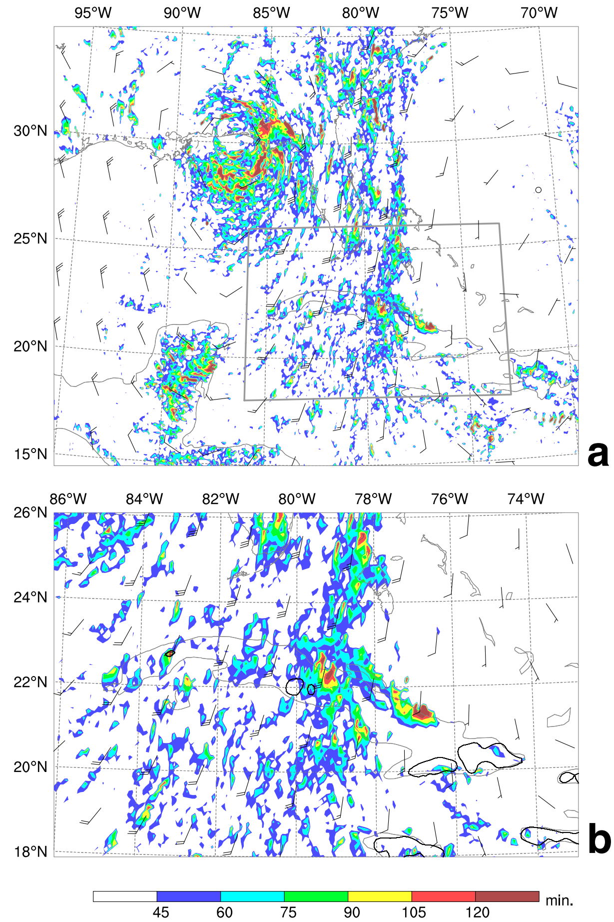

FIG. 16. Maximum cloud age on 28 May in the integration that uses deep convective cloud objects as in Fig. 14. Age is plotted in minutes as shown on the color bar, with orography, zoomed region, and mean tropospheric winds plotted as in Fig. 5.

Convective initiation is primarily controlled by the value of $c(\mathbf{X}, t)$ [Eq. (2)] in the Kain and Fritsch (1992) convection parameterization, a field that depends on both the surface type and the convective velocity scale in the GEM model. This vertical velocity forms the basis of an estimate of the temperature excess in rising thermals, and is therefore related to a property of the boundary layer circulation that should be carried with the flow rather than being instantly adjusted to surface properties. This Lagrangian view of convective initiation reduces the prevalence of coastal discontinuities in convective activity that afflict existing model configurations.

Once the convection parameterization is activated, schemes have typically held its effects constant in time and space over a specified convective adjustment period. At resolutions approaching the gray zone, convective calculations can be refreshed more frequently to account for nonequilibrium effects; however, this strategy may introduce intermittent behavior. Instead, the treatment of convective clouds as persistent objects allows for the introduction of a new branch in the triggering component of the convective scheme to represent the effects of preexisting convection. This relaxes the diagnostic triggering assumption, which is criticized by Colin et al. (2019) as being unjustifiable in systems whose time steps are shorter than the convective turnover time scale. The properties of these cloud objects can evolve as they are advected across the grid in a manner consistent with the convective life cycle.

The adoption of a Lagrangian perspective for deep convection results in precipitation patterns that appear to be more physically realistic than those generated using standard techniques under a range of conditions. This suggests that the convective memory introduced into the system through the Lagrangian framework is capable of mitigating some of the spatial and temporal inconsistencies that appear at resolutions approaching and within the convective gray zone.

One desirable attribute of the formulation described here is that it is conceptually independent of the details

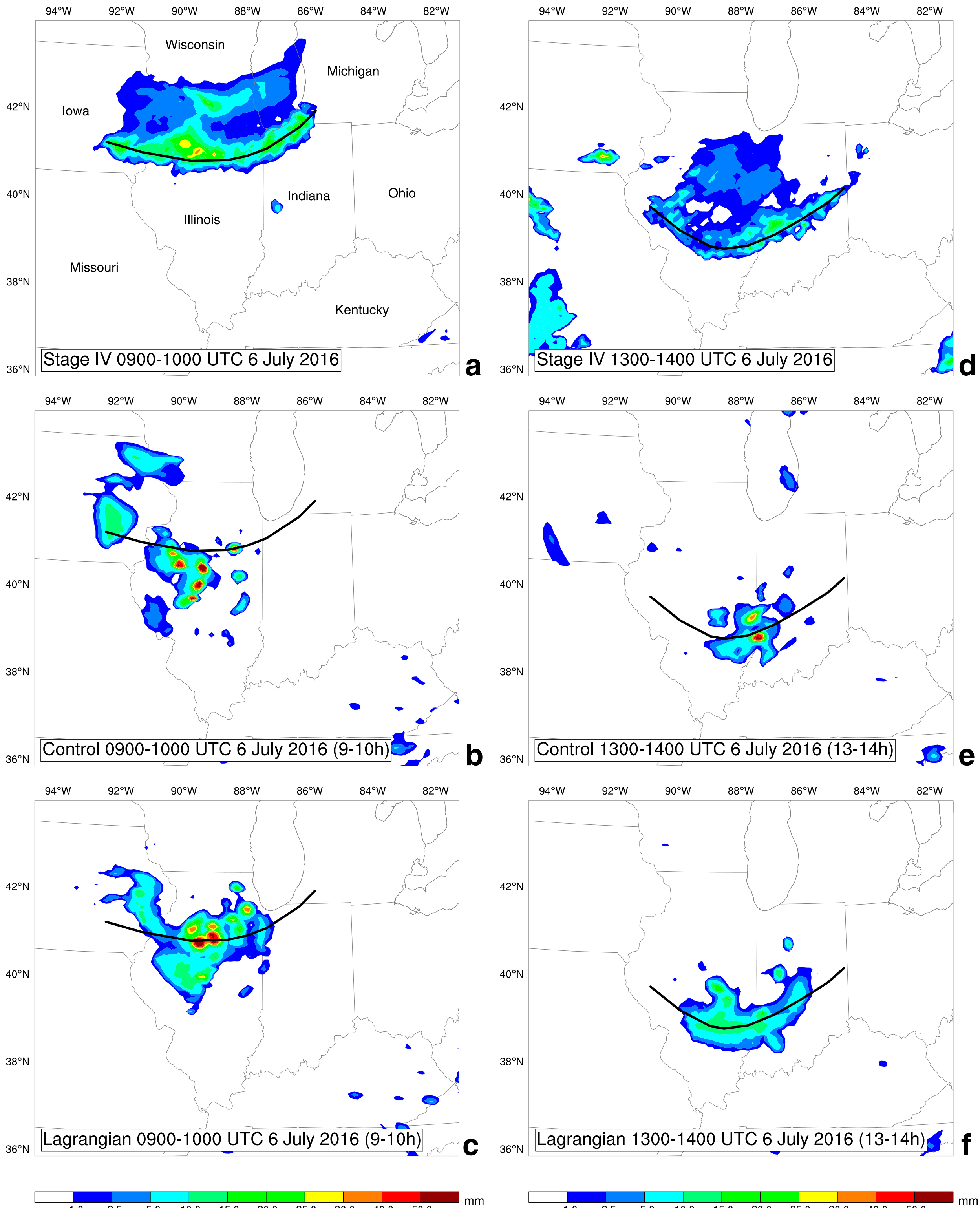

FIG. 17. The 1-h precipitation accumulations for (left) 0900 to 1000 UTC and (right) 1300 to 1400 UTC 6 Jul 2016. (a),(d) The Stage-IV analysis produced by the U.S. River Forecast Centers, (b),(e) the results of the control configuration, and (c),(f) those of an integration that uses the proposed Lagrangian framework for deep convection are shown. A heavy solid contour approximating the observed squall line maximum is plotted in each panel to facilitate comparison.

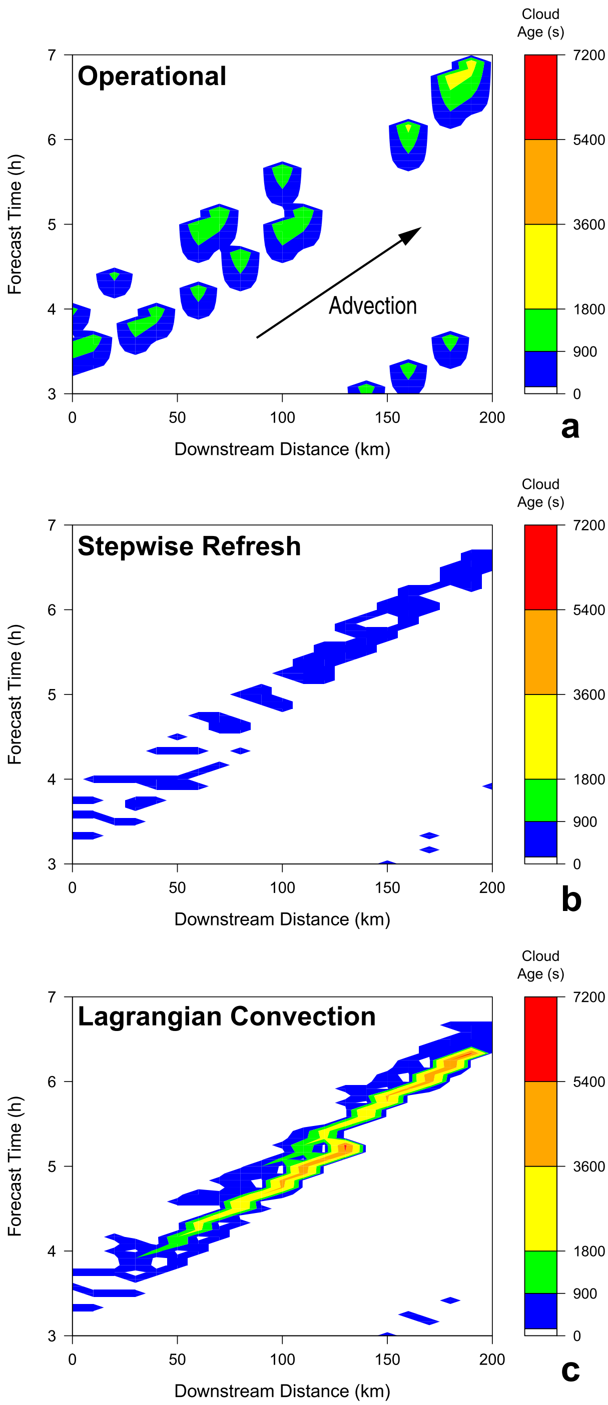

FIG. 18. Representation of convection in a weakly unstable environment under strong flow conditions (Fig. 3), shown as cloud age (color shaded in seconds as shown on the color bars) Hovmöller plots in which the abscissa is aligned with the flow. (a) Results from an integration using the currently operational configuration of the convection scheme, (b) those of a simulation with stepwise refreshment of the convection calculations ($\tau_a = 300$ s), and (c) those obtained when the Lagrangian framework for deep convection is adopted.

of the convection parameterization itself (Fig. 13). Modifications are required within the trigger function to adapt to an advected triggering variable [analogous to $c(\mathbf{X}, t)$ discussed here] and to develop a second branch to represent preexisting convection. The cloud model, solver for the mass flux equations (if applicable), and closure remain untouched. This suggests that the Lagrangian viewpoint can be adopted in a range of modeling systems as they move toward the gray zone without any fundamental changes to the nature of existing convection schemes. The increase in computational cost associated with the Lagrangian framework is negligible in the GEM model, consisting primarily of one additional advected variable related to initiation [Eq. (6)]. The treatment of the cloud objects themselves, including their displacement, incurs a cost that is smaller than typical run-to-run performance variability.

The ability of cloud objects to retain information about the maturity of convective elements paves the way to representing the deep convective life cycle in a much more refined manner. In conventional equilibrium schemes, convective clouds mature immediately upon triggering and remain mature at the grid point until they disappear at the end of the convective adjustment period. Information about the cloud age could be used in the future to control the growth, maintenance and decay of convective clouds, for example through the modulation of entrainment and detrainment rates in the cloud model or downdraft calculations (Mapes and Neale 2011) These processes could affect the evolution of a prognostic updraft profile (Gerard and Geleyn 2005) to reinforce cloud memory effects across all stages of the convective life cycle. The importance of representing subgrid-scale quantities more generally as the sources of convective memory has been demonstrated by Davies et al. (2013). Pushing the concept even further, cloud objects could be freed from the underlying model grid entirely: clouds could affect grid cells within a radius of influence through tendencies while their properties evolve as they progress through the domain. The exciting potential for the extension of the Lagrangian framework to represent the convective life cycle in a physically realistic way has not been explored in the context of the current work but is a high priority for future study.

Parameterization schemes that attempt to represent the convective life cycle may further benefit from cloud object information that represents features and processes occurring at scales much finer than the cloud itself. For example, one ongoing effort involves the introduction of an advanced microphysics scheme

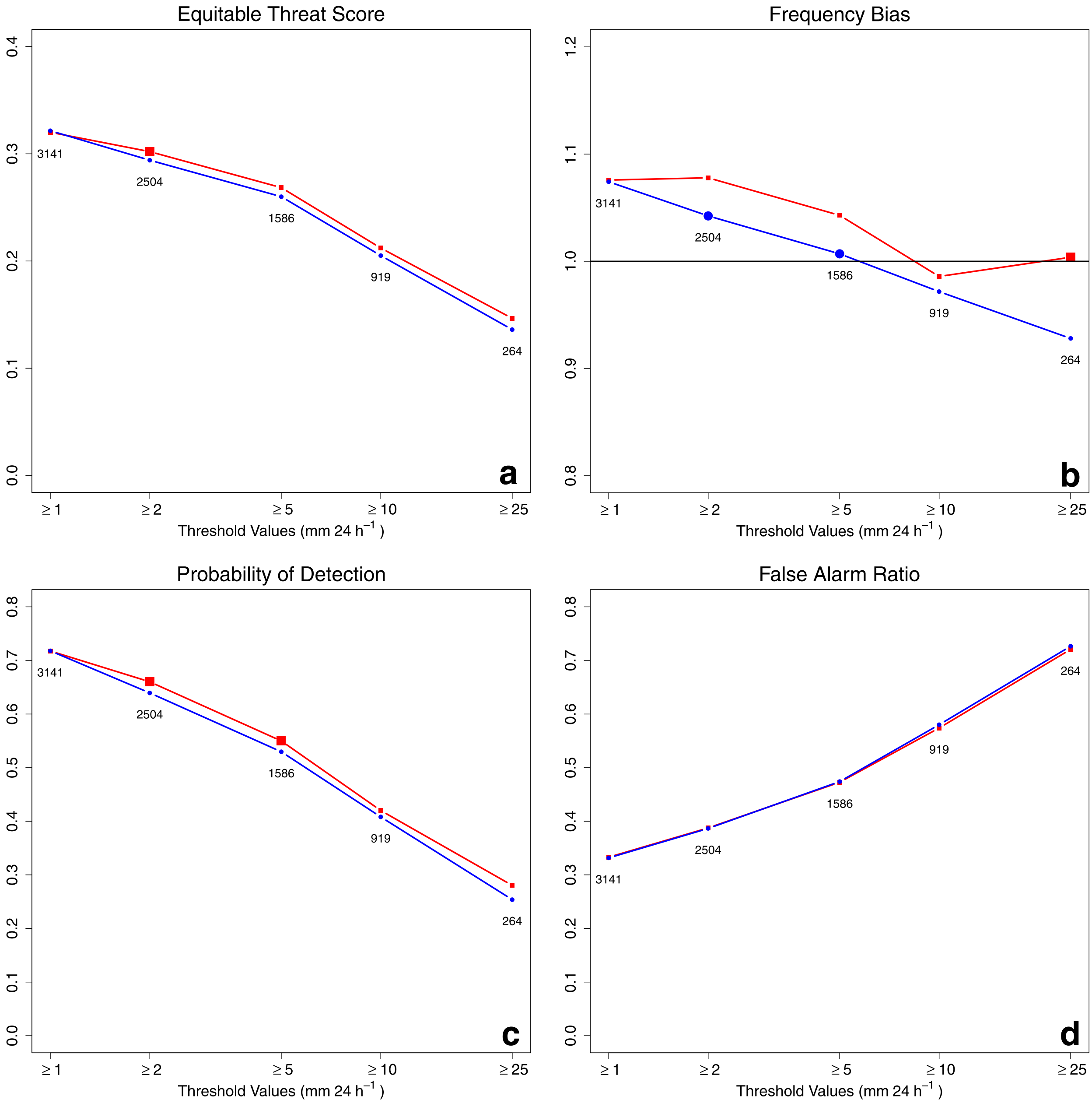

FIG. 19. Objective precipitation scores for a forecast sequence comprising 22 1200 UTC (morning) initializations at 3-day intervals between mid-June and mid-August 2016. Model precipitation estimates are compared with rain gauge observations made at synoptic stations across the United States. In each panel, scores for the control configuration are shown in blue, while those of a forecast sequence that adopts the Lagrangian framework for deep convection are shown in red. Objective scores based on 24-h precipitation accumulation thresholds (mm) for day-2 forecast period (24–48 h lead times) are (a) the equitable threat score, (b) the frequency bias, (c) the probability of detection, and (d) the false alarm ratio. The number of observations at each threshold is shown below the plotted scores, and differences between the samples that are statistically significant at the 90% level using a bootstrap test are indicated with a heavy plotting character for the configuration that yields the better score.

within a convective parameterization for the purposes of climate simulation (J. Milbrandt, personal communication). In such a scheme, detailed information about hydrometeor mass and number concentrations could evolve throughout the convective life cycle while being advected as part of the cloud object. Such a merging of refinements to convective parameterization has the potential to lead to new innovations that will improve our ability to represent moist processes in the convective gray zone.

Acknowledgments. The authors thank Peter Bechtold for his comments on an earlier draft of this study, and Holger Tost and Jason Milbrandt for discussions regarding potential extensions of the work, particularly with respect to cloud physics within the cloud object framework. We also appreciate the efforts of Almut Gassmann (*Monthly Weather Review* editor) and of a pair of reviewers who helped to prepare this work for publication. The TRMM data were provided by the NASA Goddard Space Flight Center, archived at the NASA GES DISC. The contributions of DJK were funded by the Natural Science and Engineering Research Council (NSERC) Grant NSERC/RGPIN 418372-17.

REFERENCES

Ancell, B. C., A. Bogusz, M. J. Lauridsen, and C. J. Nauert, 2018: Seeding chaos: the dire consequences of numerical noise in NWP perturbation experiments. *Bull. Amer. Meteor. Soc.*, **99**, 615–628, https://doi.org/10.1175/BAMS-D-17-0129.1.

Arakawa, A., 2004: The cumulus parameterization problem: Past, present and future. *J. Climate*, **17**, 2493–2525, https://doi.org/10.1175/1520-0442(2004)017<2493:RATCPP>2.0.CO;2.

——, and W. H. Shubert, 1974: Interactions of a cumulus ensemble with the large-scale environment, Part I. *J. Atmos. Sci.*, **31**, 674–701, https://doi.org/10.1175/1520-0469(1974)031<0674:IOACCE>2.0.CO;2.

——, and W. H. Schubert, 2011: Multiscale modeling of the moist-convective atmosphere—A review. *Atmos. Res.*, **102**, 263–285, https://doi.org/10.1016/j.atmosres.2011.08.009.

——, and C.-M. Wu, 2013: A unified representation of deep moist convection in numerical modeling of the atmosphere. Part I. *J. Atmos. Sci.*, **70**, 1977–1992, https://doi.org/10.1175/JAS-D-12-0330.1.

Bechtold, P., E. Bazile, F. Guichard, P. Mascart, and E. Richard, 2001: A mass-flux convection scheme for regional and global models. *Quart. J. Roy. Meteor. Soc.*, **127**, 869–886, https://doi.org/10.1002/qj.49712757309.

——, M. Köhler, T. Jung, F. Doblas-Reyes, M. Leutbecher, M. J. Rodwell, F. Vitart, and G. Balsamo, 2008: Advances in simulating atmospheric variability with the ECMWF model: From synoptic to decadal time scales. *Quart. J. Roy. Meteor. Soc.*, **134**, 1337–1351, https://doi.org/10.1002/qj.289.

Bélair, S., L.-P. Crevier, J. Mailhot, B. Bilodeau, and Y. Delage, 2003a: Operational implementation of the ISBA land surface scheme in the Canadian regional weather forecast model. Part I: Warm season results. *J. Hydrometeor.*, **4**, 352–370, https://doi.org/10.1175/1525-7541(2003)4<352:OIOTIL>2.0.CO;2.

——, R. Brown, J. Mailhot, B. Bilodeau, and L.-P. Crevier, 2003b: Operational implementation of the ISBA land surface scheme in the Canadian regional weather forecast model. Part II: Cold season results. *J. Hydrometeor.*, **4**, 371–386, https://doi.org/10.1175/1525-7541(2003)4<371:OIOTIL>2.0.CO;2.

——, J. Mailhot, C. Girard, and P. Vaillancourt, 2005: Boundary layer and shallow cumulus clouds in a medium-range forecast of a large-scale weather system. *Mon. Wea. Rev.*, **133**, 1938–1960, https://doi.org/10.1175/MWR2958.1.

Berg, R., 2018: National Hurricane Center tropical cyclone report: Tropical Storm Alberto (25–31 May 2018). Tech. Rep. AL012018, National Hurricane Center, 44 pp., https://www.nhc.noaa.gov/data/tcr/AL012018_Alberto.pdf.

Bougeault, P., and J. F. Geleyn, 1989: Some problems of closure assumption and scale dependency in the parameterization of moist deep convection for numerical weather prediction. *Meteor. Atmos. Phys.*, **40**, 123–135, https://doi.org/10.1007/BF01027471.

——, and P. Lacarrère, 1989: Parameterization of orography-induced turbulence in a mesobeta-scale model. *Mon. Wea. Rev.*, **117**, 1872–1890, https://doi.org/10.1175/1520-0493(1989)117<1872:POOITI>2.0.CO;2.

Bryan, G. H., and H. Morrison, 2012: Sensitivity of a simulated squall line to horizontal resolution and parameterization of microphysics. *Mon. Wea. Rev.*, **140**, 202–225, https://doi.org/10.1175/MWR-D-11-00046.1.

——, J. C. Wyngaard, and J. M. Fritsch, 2003: Resolution requirements for the simulation of deep moist convection. *Mon. Wea. Rev.*, **131**, 2394–2416, https://doi.org/10.1175/1520-0493(2003)131<2394:RRFTSO>2.0.CO;2.

Bullock, O. R., K. Alpaty, J. A. Herwehe, and J. S. Kain, 2015: A dynamically computed convective time scale for the Kain–Fritsch convective parameterization scheme. *Mon. Wea. Rev.*, **143**, 2105–2120, https://doi.org/10.1175/MWR-D-14-00251.1.

Charney, J. G., and N. A. Phillips, 1953: Numerical integration of the quasigeostrophic equations for barotropic and simple baroclinic flows. *J. Meteor.*, **10**, 71–99, https://doi.org/10.1175/1520-0469(1953)010<0071:NIOTQG>2.0.CO;2.

Cohen, B. G., and G. C. Craig, 2006: Fluctuations in an equilibrium convective ensemble. Part II: Numerical experiments. *J. Atmos. Sci.*, **63**, 2005–2015, https://doi.org/10.1175/JAS3710.1.

Colin, M., S. Sherwood, O. Geoffroy, S. Bony, and D. Fuchs, 2019: Identifying the sources of convective memory in cloud-resolving simulations. *J. Atmos. Sci.*, **76**, 947–962, https://doi.org/10.1175/JAS-D-18-0036.1.

Corfidi, S. F., J. H. Merritt, and J. M. Fritsch, 1996: Predicting the movement of mesoscale convective complexes. *Wea. Forecasting*, **11**, 41–46, https://doi.org/10.1175/1520-0434(1996)011<0041:PTMOMC>2.0.CO;2.

Craig, C., and A. Dörnbrack, 2008: Entrainment in cumulus clouds: What resolution is cloud-resolving? *J. Atmos. Sci.*, **65**, 3978–3988, https://doi.org/10.1175/2008JAS2613.1.

da Rocha, R. P., M. S. Reboita, L. F. Gozzo, L. M. Dutra, and E. M. Jesus, 2019: Subtropical cyclones over the oceanic basins: A review. *Ann. N. Y. Acad. Sci.*, **1436**, 138–156, https://doi.org/10.1111/nyas.13927.

Davies, L., R. S. Plant, and S. H. Derbyshire, 2009: A simple model of convection with memory. *J. Geophys. Res.*, **114**, D17202, https://doi.org/10.1029/2008JD011653.

——, ——, and ——, 2013: Departures from convective equilibrium with a rapidly varying surface forcing. *Quart. J. Roy. Meteor. Soc.*, **139**, 1731–1746, https://doi.org/10.1002/qj.2065.

Davis, C., and L. F. Bosart, 2004: The TT problem: Forecasting the tropical transition of cyclones. *Bull. Amer. Meteor. Soc.*, **85**, 1657–1662, https://doi.org/10.1175/BAMS-85-11-1657.

Evans, J. L., and M. P. Guishard, 2009: Atlantic subtropical storms: Part I: Diagnostic criteria and composite analysis. *Mon. Wea. Rev.*, **137**, 2065–2080, https://doi.org/10.1175/2009MWR2468.1.

Field, P., and Coauthors, 2017: Exploring the convective grey zone with regional simulations of a cold air outbreak. *Quart. J. Roy. Meteor. Soc.*, **143**, 2537–2555, https://doi.org/10.1002/qj.3105.

Fritsch, J. M., and C. F. Chappell, 1980: Numerical prediction of convectively driven mesoscale pressure systems. Part I: Convective parameterization. *J. Atmos. Sci.*, **37**, 1722–1733, https://doi.org/10.1175/1520-0469(1980)037<1722:NPOCDM>2.0.CO;2.

——, and J. Kain, 1993: Convective parameterization for mesoscale models: The Fritsch–Chappel scheme. *The Representation of Cumulus Convection in Numerical Models of the Atmosphere*, *Meteor. Monogr.*, No. 46, Amer. Meteor. Soc., 159–164.

Gerard, L., 2015: Bulk mass-flux perturbation formulation for a unified approach of deep convection at high resolution. *Mon. Wea. Rev.*, **143**, 4038–4063,https://doi.org/10.1175/MWR-D-15-0030.1.

——, and J.-F. Geleyn, 2005: Evolution of a subgrid deep convection parameterization in a limited-area model with increasing resolution. *Quart. J. Roy. Meteor. Soc.*, **131**, 2293–2312, https://doi.org/10.1256/qj.04.72.

——, J.-M. Piriou, R. Brožková, J.-F. Geleyn, and D. Banciu, 2009: Cloud and precipitation parameterization in a meso-gamma-scale operational weather prediction model. *Mon. Wea. Rev.*, **137**, 3960–3977, https://doi.org/10.1175/2009MWR2750.1.

Girard, C., and Coauthors, 2014: Staggered vertical discretization of the Canadian Global Environmental Multiscale (GEM) model using a coordinate of the log-hydrostatic-pressure type. *Mon. Wea. Rev.*, **142**, 1183–1196, https://doi.org/10.1175/MWR-D-13-00255.1.

Goddard Earth Sciences Data and Information Services Center, 2016: TRMM (TMPA) Precipitation L3 1 day 0.25 degree $\times$ 0.25 degree V7. Goddard Earth Sciences Data and Information Services Center (GES DISC), accessed 23 January 2019, https://pmm.nasa.gov/data-access/downloads/trmm.

Grell, G. A., and S. R. Freitas, 2014: A scale and aerosol aware stochastic convective parameterization for weather and air quality modeling. *Atmos. Chem. Phys.*, **14**, 5233–5250, https://doi.org/10.5194/acp-14-5233-2014.

Han, J., W. Wang, Y. C. Kwon, S. Hong, V. Tallapragada, and F. Yang, 2017: Updates in the NCEP GFS cumulus convection schemes with scale and aerosol awareness. *Wea. Forecasting*, **32**, 2005–2017, https://doi.org/10.1175/WAF-D-17-0046.1.

Hennon, C. C., and Coauthors, 2013: Tropical cloud cluster climatology, variability, and genesis productivity. *J. Climate*, **26**, 3046–3066, https://doi.org/10.1175/JCLI-D-12-00387.1.

Hong, S.-Y., and J. Dudhia, 2012: Next-generation numerical weather prediction: Bridging parameterization, explicit clouds, and large eddies. *Bull. Amer. Meteor. Soc.*, **93**, ES6–ES9, https://doi.org/10.1175/2011BAMS3224.1.

Houze, R. A., 1994: *Cloud Dynamics*. Elsevier, 573 pp.

Jones, T. R., and D. A. Randall, 2011: Quantifying the limits of convective parameterization. *J. Geophys. Res.*, **116**, D08210, https://doi.org/10.1029/2010JD014913.

Kain, J. S., 2004: The Kain–Fritsch convective parameterization: An update. *J. Appl. Meteor.*, **43**, 170–181, https://doi.org/10.1175/1520-0450(2004)043<0170:TKCPAU>2.0.CO;2.

——, and J. M. Fritsch, 1990: A one-dimensional entraining/detraining plume model and its application in convective parameterization. *J. Atmos. Sci.*, **47**, 2784–2802, https://doi.org/10.1175/1520-0469(1990)047<2784:AODEPM>2.0.CO;2.

——, and ——, 1992: The role of the convective ''trigger'' function in numerical forecasts of mesoscale convective systems. *Meteor. Atmos. Phys.*, **49**, 93–106, https://doi.org/10.1007/BF01025402.

——, and ——, 1993: Convective parameterization for mesoscale models: The Kain–Fritsch scheme. *The Representation of Cumulus Convection in Numerical Models of the Atmosphere*, *Meteor. Monogr.*, No. 46, Amer. Meteor. Soc., 165–170.

Kirshbaum, D. J., and R. B. Smith, 2009: Orographic precipitation in the tropics: Large-eddy simulations and theory. *J. Atmos. Sci.*, **66**, 2559–2578, https://doi.org/10.1175/2009JAS2990.1.

Kuell, V., A. Gassmann, and A. Bott, 2007: Towards a new hybrid cumulus parameterization scheme for use in non-hydrostatic weather prediction models. *Quart. J. Roy. Meteor. Soc.*, **133**, 479–490, https://doi.org/10.1002/qj.28.

Li, J., and H. W. Barker, 2005: A radiation algorithm with correlated-k distribution. Part I: Local thermal equilibrium. *J. Atmos. Sci.*, **62**, 286–309, https://doi.org/10.1175/JAS-3396.1.

Lock, A., and J. Mailhot, 2006: Combining non-local scalings with a TKE closure for mixing in boundary-layer clouds. *Bound.-Layer Meteor.*, **121**, 313–338, https://doi.org/10.1007/s10546-006-9062-8.

Mapes, B., 1997: Equilibrium vs. activation control on large-scale variations of tropical deep convection. *The Physics and Parameterization of Moist Atmospheric Convection*, R. K. Smith, Ed., Vol. 505, Springer, 321–358, https://doi.org/10.1007/978-94-015-8828-7_13.

——, and R. Neale, 2011: Parameterizing convective organization to escape the entrainment dilemma. *J. Adv. Model. Earth Syst.*, **3**, M06004, https://doi.org/10.1029/2011MS000042.

McFarlane, N. A., 1987: The effect of orographically excited gravity wave drag on the general circulation of the lower stratosphere and troposphere. *J. Atmos. Sci.*, **44**, 1775–1800, https://doi.org/10.1175/1520-0469(1987)044<1775:TEOOEG>2.0.CO;2.

Molinari, J., and M. Dudek, 1992: Parameterization of convective precipitation in mesoscale numerical models: A critical review. *Mon. Wea. Rev.*, **120**, 326–344, https://doi.org/10.1175/1520-0493(1992)120<0326:POCPIM>2.0.CO;2.

Noilhan, J., and S. Planton, 1989: A simple parameterization of land surface processes for meteorological models. *Mon. Wea. Rev.*, **117**, 536–549, https://doi.org/10.1175/1520-0493(1989)117<0536:ASPOLS>2.0.CO;2.

Ogura, Y., and H.-R. Cho, 1973: Diagnostic determination of cumulus cloud populations from observed large-scale variabilities. *J. Atmos. Sci.*, **30**, 1276–1286, https://doi.org/10.1175/1520-0469(1973)030<1276:DDOCCP>2.0.CO;2.

Pan, D.-M., and D. A. Randall, 1998: A cumulus parameterization with a prognostic closure. *Quart. J. Roy. Meteor. Soc.*, **124**, 949–981, https://doi.org/10.1002/qj.49712454714.

Seidel, D. J., Y. Zhang, A. Beljaars, J.-C. Golaz, A. R. Jacobson, and B. Medeiros, 2012: Climatology of the planetary boundary layer over the continental United States and Europe. *J. Geophys. Res.*, **117**, D17106, https://doi.org/10.1029/2012JD018143.

Soderholm, B., B. Ronalds, and D. J. Kirshbaum, 2014: The evolution of convective storms initiated by an isolated mountain ridge. *Mon. Wea. Rev.*, **142**, 1430–1451, https://doi.org/10.1175/MWR-D-13-00280.1.

Steppeler, J., G. Doms, U. Schättler, H. W. Bitzer, A. Gassmann, U. Damrath, and G. Gregoric, 2003: Meso-gamma scale forecasts using the nonhydrostatic model LM. *Meteor. Atmos. Phys.*, **82**, 75–96, https://doi.org/10.1007/s00703-001-0592-9.

Stevens, D. E., A. S. Ackerman, and C. S. Bretherton, 2002: Effects of domain size and numerical resolution on the simulation of shallow cumulus convection. *J. Atmos. Sci.*,

59, 3285–3301, https://doi.org/10.1175/1520-0469(2002)059<3285:EODSAN>2.0.CO;2.

Sundqvist, H., E. Berge, and J. E. Kristjánsson, 1989: Condensation and cloud parameterization studies with a mesoscale numerical weather prediction model. *Mon. Wea. Rev.*, **117**, 1641–1657, https://doi.org/10.1175/1520-0493(1989)117<1641:CACPSW>2.0.CO;2.

Tiedtke, M., 1989: A comprehensive mass flux scheme for cumulus parameterization in large scale models. *Mon. Wea. Rev.*, **117**, 1779–1799, https://doi.org/10.1175/1520-0493(1989)117<1779:ACMFSF>2.0.CO;2.

Tomassini, L., P. R. Field, R. Honnert, S. Malardel, R. McTaggart-Cowan, K. Saitou, A. T. Noda, and A. Siefert, 2017: The ''grey zone'' cold air outbreak global model intercomparison: A cross evaluation using large-eddy simulations. *J. Adv. Model. Earth Syst.*, **9**, 39–64, https://doi.org/10.1002/2016MS000822.

Weisman, M. L., and J. B. Klemp, 1982: The dependence of numerically simulated convective storms on vertical wind shear and buoyancy. *Mon. Wea. Rev.*, **110**, 504–520, https://doi.org/10.1175/1520-0493(1982)110<0504:TDONSC>2.0.CO;2.

Wyngaard, J. C., 2004: Toward numerical modeling in the ''terra incognita.'' *J. Atmos. Sci.*, **61**, 1816–1826, https://doi.org/10.1175/1520-0469(2004)061<1816:TNMITT>2.0.CO;2.

Zadra, A., M. Roch, S. Laroche, and M. Charron, 2003: The subgrid scale orographic blocking parametrization of the GEM model. *Atmos.–Ocean*, **41**, 155–170, https://doi.org/10.3137/ao.410204.

——, R. McTaggart-Cowan, P. A. Vaillancourt, M. Roch, S. Bélair, and A.-M. Leduc, 2014: Evaluation of tropical cyclones in the Canadian global modeling system: Sensitivity to moist process parameterization. *Mon. Wea. Rev.*, **142**, 1197–1220, https://doi.org/10.1175/MWR-D-13-00124.1.

Zeng, X., and A. Beljaars, 2005: A prognostic scheme of sea surface skin temperature for modeling and data assimilation. *Geophys. Res. Lett.*, **32**, L14605, https://doi.org/10.1029/2005GL023030.

Zimmer, M., G. C. Craig, C. Keil, and H. Wernli, 2011: Classification of precipitation events with a convective response timescale and their forecasting characteristics. *Geophys. Res. Lett.*, **38**, L05802, https://doi.org/10.1029/2010GL046199.